Device

Article

Embodying mechano-fluidic memory in soft machines to program behaviors upon interactions

Graphical abstract

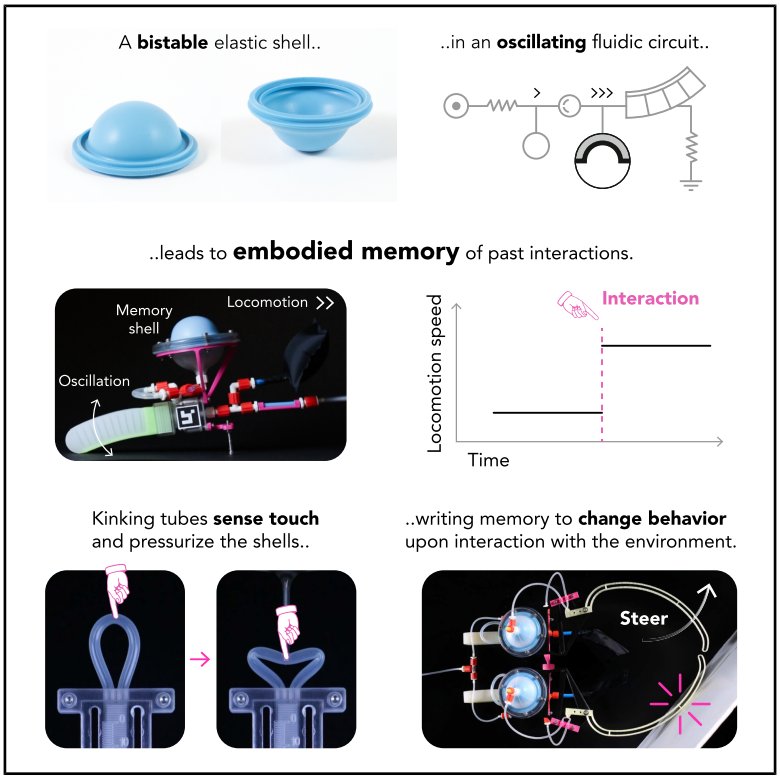

Highlights

- A bistable elastic shell introduces embodied memory in soft fluidic machines
- Fluidic circuits around the shell lead to both long- and short-term memory
- Kinking tubes as fluidic antennae allow the machines to sense the external world
- A mechano-fluidic machine with shells and antennae avoids obstacles on its own

Authors

Alberto Comoretto, Stijn Koppen, Tanaya Mandke, Johannes T. B. Overvelde

Correspondence

overvelde@amolf.nl

In brief

We show that bistable elastic shells enable the embodiment of mechano-fluidic memory in soft machines. Each stable state of the shell leads to a stable locomotion frequency of a self-oscillating soft fluidic machine. When provided with antennae in which tubes kink and unkink, the machines can write the memory states upon external interactions. Embodying memory in their physical structure allows soft machines to remember past events (for example, to avoid obstacles by remembering their detection), in addition to passively responding to them.

2 Explore
Early prototypes with exciting performance and new methodology

Comoretto et al., 2025, Device *3*, 100863
October 17, 2025
Published by Elsevier Inc.
https://doi.org/10.1016/j.device.2025.100863

CellPress

Please cite this article in press as: Comoretto et al., Embodying mechano-fluidic memory in soft machines to program behaviors upon interactions, Device (2025), https://doi.org/10.1016/j.device.2025.100863

Device

CellPress
OPEN ACCESS

Article

Embodying mechano-fluidic memory in soft machines to program behaviors upon interactions

Alberto Comoretto,[1] Stijn Koppen,[1] Tanaya Mandke,[1] and Johannes T.B. Overvelde[1,2,*]
[1]Autonomous Matter Department, AMOLF, Science Park 104, 1098 XG Amsterdam, the Netherlands
[2]Lead contact
*Correspondence: overvelde@amolf.nl
https://doi.org/10.1016/j.device.2025.100863

THE BIGGER PICTURE Animals show richness in adopted behaviors, which are programmed based on interactions with the external world. For instance, the nematode *Caenorhabditis elegans* switches between fundamental locomotion modes, such as moving straight and steering, based on the history of external cues and the current surroundings. Soft machines already show feats of passive deformation to external cues. Could a soft machine also remember past interactions using its body, without a processor? We harness the bistability of elastic shells to embody mechano-fluidic memory in soft machines. By storing information of past cues from the external world in their physical body, the machines program new stable locomotion behaviors. When provided with antennae where soft tubes kink and unkink, the machines with embodied memory can detect and avoid obstacles in unknown environments by switching between moving straight and steering, all without software or processors. Embodied memory opens the door to robust, autonomous behaviors that are fully embedded in the nonlinear mechanical structure the machines are made of, for applications ranging from responsive microrobots to reliable space exploration in harsh weather.

SUMMARY

Soft machines display shape adaptation to external circumstances due to their intrinsic compliance. To achieve increasingly responsive behaviors upon interactions without relying on centralized computation, embodying memory directly in the machines' structure is crucial. Here, we harness the bistability of elastic shells to alter the fluidic properties of an enclosed cavity, thereby switching between stable frequency states of a locomoting self-oscillating machine. To program these memory states upon interactions, we develop fluidic circuits surrounding the bistable shell, with soft tubes that kink and unkink when externally touched. We implement circuits for both long-term and short-term memory in a soft machine that switches behaviors in response to a human user and that autonomously changes direction after detecting a wall. By harnessing only geometry and elasticity, embodying memory allows physical structures without a central brain to exhibit autonomous feats that are typically reserved for computer-based robotic systems.

INTRODUCTION

Soft robots are being developed for autonomous operation in the complex real world.[1] Often inspired by biological systems,[2] soft robots passively adapt to external stimuli due to their intrinsic compliance.[3] This passive adaptability at the level of material and structure, often called mechanical or embodied intelligence,[4] enables soft robots to accomplish tasks such as grasping a wide variety of objects using the same gripper,[5] walking over uneven terrain,[6] resisting external damage,[7,8] and even self-healing.[9]

Their natural counterparts, animals, achieve feats that are more complex than mechanical adaptation: they often dynamically change their behaviors in response to external stimuli. For instance, sea stars typically slowly explore the environment in search of food, but, when threatened by predators, they suddenly enter a fast galloping gait as an escape response.[10,11] Salamanders switch between two stable locomoting gaits: undulatory swimming in the water and slower stepping motions on the ground.[12,13] Even the relatively simple organism *Caenorhabditis elegans* switches between basic behavioral states of locomotion, such as forward moving and turning, depending on the surroundings, previous experiences, and internal factors.[14] In general, this switching of behaviors can be seen as a form of memory, where each adopted behavior is a stable memory state that depends on past events.

In an effort to provide soft machines with this kind of responsiveness, researchers developed artificial systems that harness

Please cite this article in press as: Comoretto et al., Embodying mechano-fluidic memory in soft machines to program behaviors upon interactions, Device (2025), https://doi.org/10.1016/j.device.2025.100863

structural phenomena to passively exhibit distinct behaviors depending on external cues. Mechanical robots, in which geometric nonlinearities combined with elasticity lead to reprogrammable mechanisms with multi-welled energy landscapes, continuously change the internal activation sequences as a direct response to interactions.[15] Soft twisting liquid crystal elastomers[16] and elasto-active structures[17] exploit environmental interactions and passive shape reconfiguration to solve mazes. Soft modular machines sense and respond to different external stimuli by harnessing responsive materials.[18] In previous work, we introduced soft machines with self-oscillating limbs[19] that passively tune their synchronization pattern depending on external cues through implicit coupling with the surrounding medium. These exciting initial advances point toward embodying switchable behaviors within the physical structure of the machine itself. In this direction, there is ample room for further investigation in understanding and then utilizing structural phenomena not only for mechanical shape adaptation but also for behavioral adaptation.[20]

In particular, the implementation of memory, where current behaviors depend on past stimuli,[21–28] has been explored in multistable structures such as elastic beams,[23] origami,[24] corrugated sheets,[25] and crumpled paper.[26] Multistability allows these systems to transition from one stable state to another upon applying a stimulus (for instance, at time t^*). Crucially, at a later time t when the system is in this new state and the stimulus is not applied anymore, the state is stable, and thereby it carries information of the past stimulus that occurred at time $t^* < t$. This kind of memory remains largely unexplored in locomoting soft machines. Embodying memory in the physical structure of the machines would enable them to selectively program desired, stable behaviors in response to external interactions.

Focusing in this work on soft fluidic machines, fluidic circuits,[29] consisting of interconnections of pneumatic tubings[30–32] and nonlinear inflatable elements[33] and valves,[8,34–38] represent a promising platform for implementing behaviors at the centimeter scale. In fact, multiple phenomena and tools are available to designers, including viscous flow,[30,31] snap-through instabilities,[33,39,40] transistors,[41] and oscillators.[19,35,37,38,42,43] Fluidic circuits have proved effective for a variety of behaviors, including sequential activation of soft fingers,[37] self-oscillation of fully soft octopi-like dancing machines,[44] automatic gripping,[35,36] and open-loop gait control for walking robots.[19,37,39,42,45–47] Despite the progress at the component and circuitry level, integration in autonomous systems capable of responding and adapting to changing environmental circumstances remains elusive. Exceptions consist of passively following walls[19,46] and switching behavior in response to external cues only once, as seen in a walker that changes locomotion direction when obstructed,[45] and in an extensible gripper that we developed that transitions from searching to retrieving a sensed object.[48]

Here, by instilling memory in the physical body of soft fluidic machines, we enable the programmability of stable behaviors upon repeated interactions with the surroundings. We start from a soft robotic crawler, to which we provide memory by harnessing the bistability of elastic shells.[49] Through fluidic circuits that surround the shells, we show both long-term and short-term memory of touch interactions. After each interaction, the memory state is rewritten, and the response of the machine changes accordingly. Equipped with fluidic antennae, the machine detects the presence of obstacles, memorizes the information of the detection, and responds by autonomously steering away. By introducing such a physical form of memory, we expand the repertoire of design tools for autonomous soft machines,[15–19] which can now remember interactions after they occur in addition to passively responding to them.

RESULTS

A self-oscillating soft fluidic machine

We start by designing a self-oscillating locomoting machine consisting of a single pneumatic bending actuator (Figure 1A). Given a constant pressure source, the machine crawls in a pulsatile fashion, because it is cyclically activated through a hysteretic valve, mounted inside the machine, previously developed in our group.[37,43] Given constant inflow, the valve oscillates between a closed state (Figure 1B) and an open state (Figure 1C). While oscillating, the valve goes through several stages (Figure S1). (1) When closed, no air flow is delivered to the actuator, and pressure upstream increases. (2) When a critical pressure is reached, the valve snaps to the open state, allowing flow to the actuator, decreasing pressure upstream. (3) When a low critical pressure difference is reached, the valve snaps back to the closed state. This hysteresis in opening and closing results in cyclic inflation and deflation of the actuator, leading to forward locomotion.

The fluidic circuit carried by, and activating, the machine (Figure 1D) is characterized by six key physical parameters. (1) The pressure source value together with the (2) pre-resistance R_{pre} determine the amount of inflow to the valve. That is, both a larger pressure source and a smaller pre-resistance lead to higher inflow. (3) The pre-capacitance with volume V_{pre} is responsible for the timescale of charging, where larger volume leads to longer charging. After the valve, we place (4) the actuator that acts as a capacitance with geometric volume $V_{actuator}$, (5) the after-capacitance with volume V_{after}, and (6) the after-resistance R_{after}, responsible for the amount of inflation of the actuator and the discharge time.[37]

Note that we refer to flow constrictions as resistances and air chambers as capacitances. This fluidic-electrical analogy[37,50] consists of treating pressure as voltage and flow as current. This analogy across domains allows us to intuitively model, and consequently understand, the behavior of the various fluidic circuits that we introduce in the article, using electrical LTspice models. We refer to Note S1 for a detailed explanation of the theory behind the analogy. In particular, the analogy allows us to formulate a formal definition of the fluidic capacitance for a stiff chamber as $C = V/K$, with V the geometric volume of the chamber and K the bulk modulus of the gas,[51] which, for ideal gases, equals the gas pressure. Hence, for sufficiently stiff elements, the geometric volume of the chamber directly affects the capacitance value when embedded in a fluidic circuit. For this reason, from now on, we will refer to volume as the main physical property of a capacitance.

Practically, we build the pre-resistor as a custom-made silicone tube with a small inner diameter of 0.35 mm, outer diameter

Please cite this article in press as: Comoretto et al., Embodying mechano-fluidic memory in soft machines to program behaviors upon interactions, Device (2025), https://doi.org/10.1016/j.device.2025.100863

CellPress
OPEN ACCESS

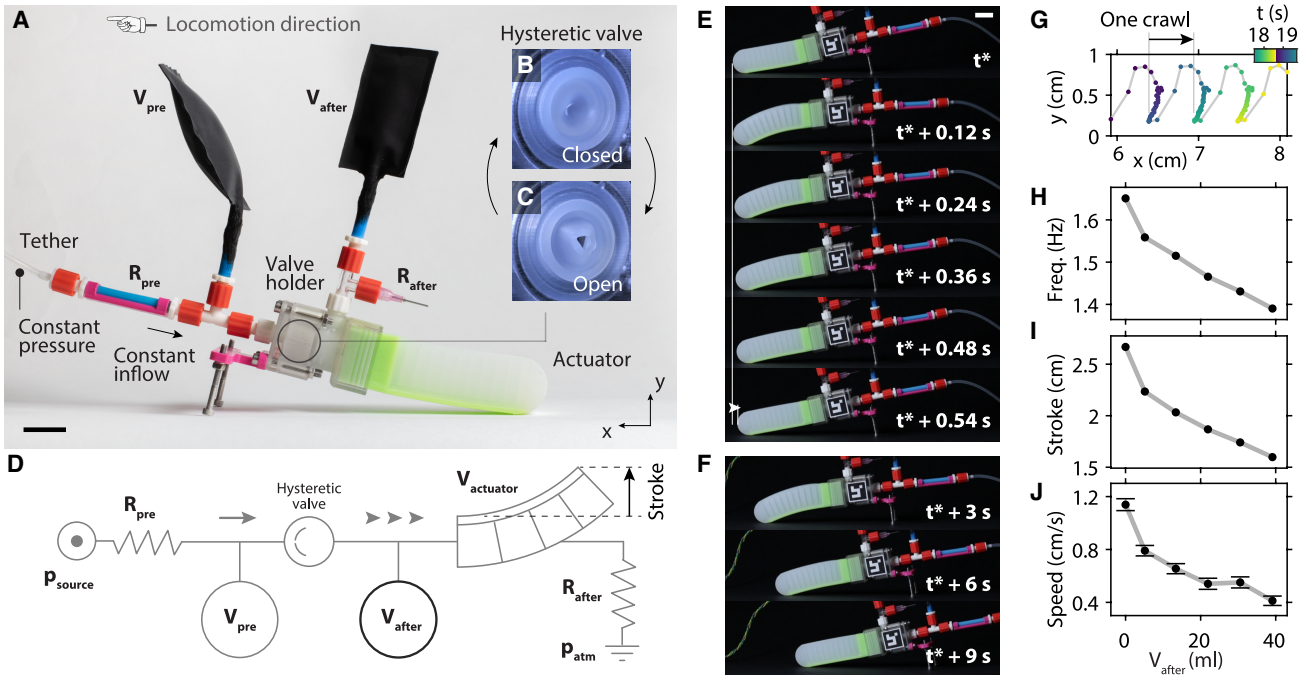

Figure 1. A self-oscillating soft fluidic machine

(A) A soft crawling machine is equipped with a bending actuator, pre- and after-capacitances (V_{pre} and V_{after}), pre- and after-resistances (R_{pre} and R_{after}), and a hysteretic valve mounted in a rigid holder. A single tether provides constant pressure to the pre-resistance.

(B and C) Given the approximately constant inflow from the pre-resistance, the soft hysteretic valve oscillates between closed (B) and open (C) states, enabling pulsatile actuation of the bending actuator.

(D) Schematic of the fluidic circuit embedded in the machine.

(E) Locomotion of the crawler during one oscillation cycle lasting 0.54 s.

(F) Location of the crawler after 3, 6, and 9 s.

(G) Horizontal and vertical coordinates of the rigid holder of the locomoting machine.

(H–J) Influence of the after-capacitance geometrical volume V_{after} on the oscillation frequency of the actuator (H), vertical stroke of the actuator as defined in (D) (I), and speed of the machine (J).

Data in (J) are reported as mean ± standard deviation. All scale bars represent 2 cm. See also Figures S1, S2, S3, and S4.

5 mm, and length 40 mm through injection molding; the after-resistor is an off-the-shelf needle (20 gauge, 0.5 in length); the capacitors are thin, inextensible pouches custom made through heat-sealing of nylon-coated thermoplastic polyurethane (TPU) sheets[52]; the pneumatic bending actuator is a two-material PneuNet custom-made through injection-molding[53] (see the methods).

The pulsatile inflation of the actuator induced by the fluidic circuit causes the machine to move forward at a speed of 0.76 cm s^{-1} (2.85 body lengths per minute) (Figures 1E and 1F) through consecutive crawling motion of ~5.3 mm each (0.03 body lengths for each cycle) (Figure 1G). This single-input crawling machine is purposefully simple in its behavior (that is, moving forward at a specific average speed). Throughout the article, we will use this unit and its associated fluidic circuit as a building block to construct more complex behaviors by adding memory and sensing features to the circuit and assembling multiple units together.

As a start, we observe that varying the physical parameters of the circuit directly results in a change of behavior of the machine. For example, in a benchtop experiment with the actuator not interacting with the ground (see the methods), increasing the volume of the after-capacitance from 0 to 40 mL results in the activation frequency decreasing from 1.65 to 1.39 Hz (Figure 1H) and the vertical stroke of the actuator lowering from 2.7 to 1.6 cm (Figure 1I). This experimental trend is qualitatively and quantitatively confirmed by an analogous electrical LTspice model (Note S1; Figures S2 and S3). This change in the volume of the after-capacitance has a direct consequence on the speed of the locomoting machine. Adding an after-capacitance with volume 40 mL causes the machine to crawl slower at 0.4 cm s^{-1}, at approximately one-third of the original speed (1.1 cm s^{-1}) (Figure 1J). Varying other physical parameters also affects the behavior. For instance, increasing the pre-capacitance from 0 to 70 mL leads to a higher vertical stroke of the actuator (Figure S4).

Embodying memory via a bistable mechano-fluidic capacitor

To introduce memory in the system, we provide bistability to a physical parameter of the self-oscillating circuit, so that the crawling behavior also becomes bistable. In our specific case, we focus on the after-capacitance, as the behavior of the machine is particularly sensitive to this parameter. This is because

Please cite this article in press as: Comoretto et al., Embodying mechano-fluidic memory in soft machines to program behaviors upon interactions, Device (2025), https://doi.org/10.1016/j.device.2025.100863

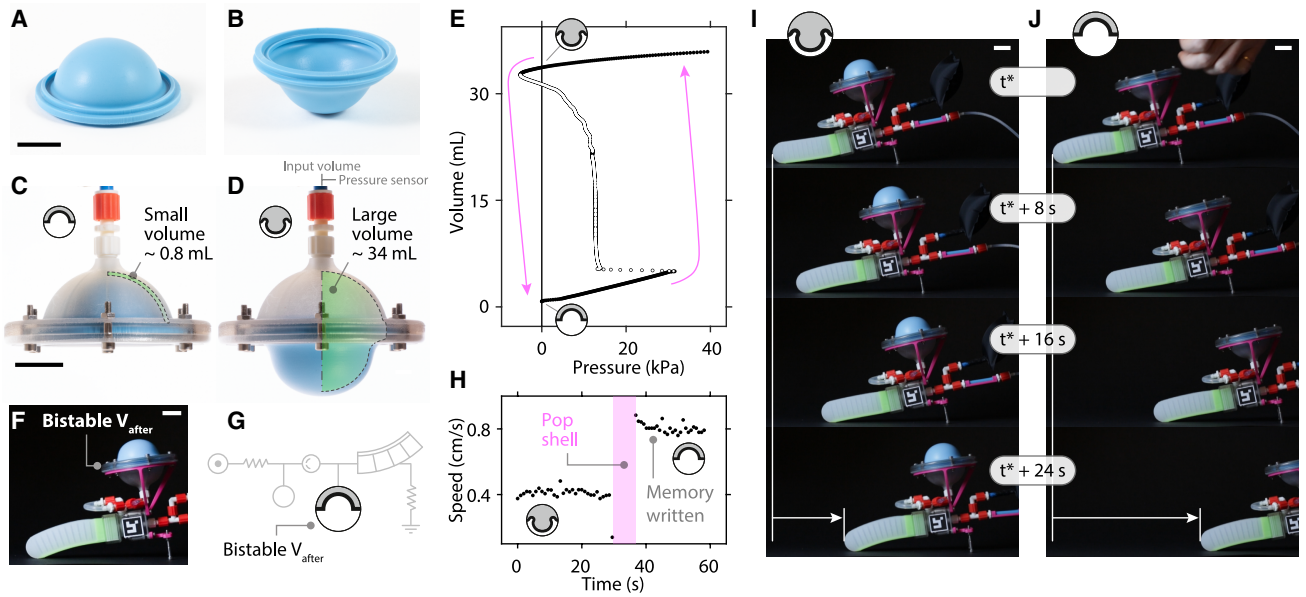

Figure 2. Embodying memory via a bistable mechano-fluidic capacitor

(A and B) An elastic shell with thickness 3 mm, base width 55 mm, and shallowness angle 80° displays two stable states: a rest state (A) and a popped state (B).

(C and D) When the soft shell is mounted on a rigid shell-shaped holder, the geometric volume between the two shells also displays two states: a small-volume state (C) and a large-volume state (D).

(E) Increasing (or decreasing) pressure above (or below) the critical snap-through (or snap-back) pressure allows for switching between the two states (pink arrows). Markers filled in white are consecutive datapoints for which pressure decreases for increasing volume, hence representing numerically the negative slope of the non-monotonic pressure-volume curve. We obtain the pressure-volume curve (see the methods) by injecting a controlled amount of water and measuring pressure as indicated in (D).

(F and G) We physically mount the bistable capacitor on top of the crawler (F), fluidically connected as an after-capacitance (G).

(H) We write the memory state by popping the shell while the machine crawls so that the machine switches from the first stable state with speed ~0.4 cm s^{-1} to the second stable state with speed ~0.8 cm s^{-1}.

(I and J) Snapshots of the crawling machine in the low-speed state (I) and in the high-speed state (J).

All scale bars represent 2 cm. See also Figure S5 and Video S1.

increasing the after-capacitance leads to a decrease in both the actuator's stroke and frequency, while increasing the pre-capacitance leads to an increase in stroke but a decrease in frequency, with a negligible net change in speed (Figure S4).

To provide bistability to the after-capacitance, we use elastic shells, as they are well-studied structures and exhibit rich nonlinear behavior.[35,49,54–59] The design parameters such as thickness, base width, and shallowness angle (Figure S5) can be tuned[35] so that the shell displays bistability,[49] with a "rest" stable state (Figure 2A) and a "snapped" stable state (Figure 2B). We mount the soft shell in a rigid shell-shaped holder, obtaining a fluidic capacitor with a relatively small (compared to the soft actuator) geometric volume of ~0.8 mL enclosed between the two shells when the elastic shell is in its rest state (Figure 2C). The second stable state of the bistable capacitor is accessed by popping the shell to the snapped state, obtaining a relatively large geometric volume (~34 mL) (Figure 2D).

The behavior of the bistable capacitor upon inflation is highly nonlinear. The pressure-volume curve of the capacitor (Figure 2E) highlights two stable regimes that cross the zero-pressure line, which is essential to enable bistability. Increasing (or decreasing) pressure past the critical snap-through (or snap-back) pressure allows for switching from one stable regime to the other (Figure 2E, pink arrows). Once the system is placed in one regime, removing pressure results in the capacitor being stable at one of the two states (0.8 or 34 mL). Note how this highly nonlinear, non-monotonic behavior fundamentally differs from capacitors (i.e., actuators) typically used in fluidic circuits.[37] Such capacitors are characterized by a monotonic pressure-volume curve, even when displaying nonlinear behaviors, such as stiffening or softening (Figure S6).

We physically mount the bistable capacitor on the crawler (Figure 2F), fluidically connected in the circuit as after-capacitance V_{after} (Figure 2G). We start by setting the bistable capacitor to the snapped state with large volume (Figure 2F). When we provide a constant pressure of 1.3 bar to the tether, the machine locomotes at a speed of ~0.4 cm s^{-1} (Figures 2H and 2I). After ~30 s, we manually pop the shell to the rest state, so that the capacitance snaps to the small-volume state (Video S1). After this external interaction, the machine is moving at a higher speed of ~0.8 cm s^{-1} (Figures 2H and 2J), as expected from Figure 1, because of the lower after-capacitance. Crucially, the bistability of the fluidic after-capacitance directly results in two stable outcome behaviors of the machine. We refer to this mechano-fluidic bistability as memory, as the state of the system at a given current time t reflects interactions that occurred in the past at time $t^* < t$.[21–28] In the example experiment in Figures 2H–2J, the speed of the machine at

Please cite this article in press as: Comoretto et al., Embodying mechano-fluidic memory in soft machines to program behaviors upon interactions, Device (2025), https://doi.org/10.1016/j.device.2025.100863

CellPress
OPEN ACCESS

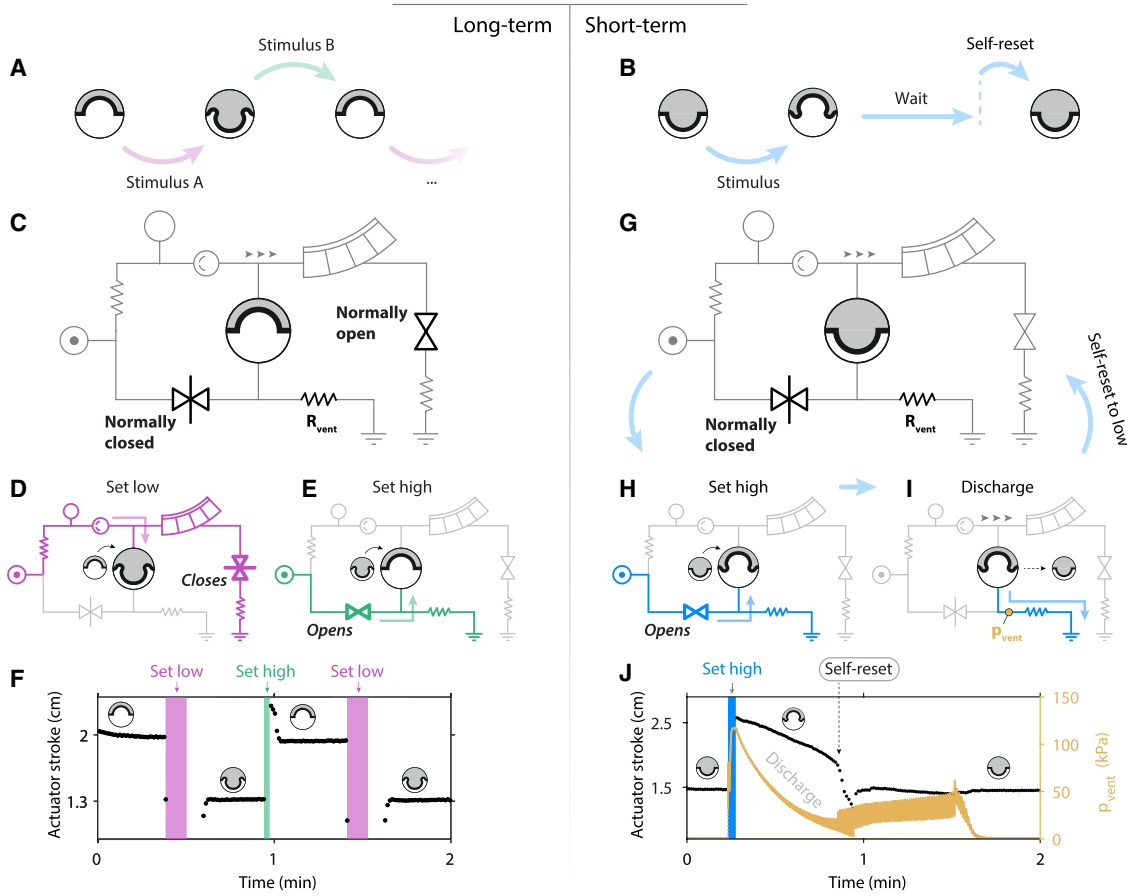

Figure 3. Fluidic circuits for writable and readable long-term and short-term memory

(A) Long-term memory involves programming stable states given occurring stimuli.

(B) Short-term memory stores information of the past stimulus for a determined amount of time and then self-resets to the initial state.

(C) The long-term memory circuit is equipped with a normally open (NO) valve, a normally closed (NC) valve, and a venting resistance R_{vent} at the bottom chamber line.

(D) We set the system to the state with low stroke and frequency (high after-capacitance) by temporarily closing the NO valve, thereby pressurizing the top chamber and snapping the shell.

(E) We set the system to the other state by temporarily opening the NC valve, resulting in snap-back of the shell.

(F) Actuator stroke in time, with consecutive events of writing memory.

(G) The short-term memory circuit is equivalent to the long-term memory circuit, with the only differences being the orientation of the shell in its rest state and the NO valve not being used.

(H) We write the memory by temporarily opening the NC valve to induce shell snapping.

(I) After this writing, the bottom chamber is pressurized (p_{vent}), and air leaks through the venting resistance, causing a pressure discharge in time, until the shell snaps back, causing a self-reset of the system to the initial state in (G).

(J) Actuator stroke (black) and p_{vent} (yellow) in time.

See also Figures S7, S8, S9, and S10, and Video S2.

time t = 60 s reflects the past interaction of popping the shell that occurred at time $t^* \approx 35$ s.

Fluidic circuits for writable and readable long-term and short-term memory

We demonstrated a bistable behavior through a mechano-fluidic memory element. So far, the memory state could be written only once by manually popping the shell from the snapped state to the rest state. In addition, we needed a relatively high external force to write the memory state (~13 N, given the surface area of the human thumb ~3.2 cm^2[60] and the internal pressure ~40 kPa). We now aim to repeatably change behavior upon consecutive limited-power interactions with the environment. We develop fluidic circuits around the bistable capacitor to obtain long-term memory (Figure 3A) and short-term memory (Figure 3B) that require lower power to switch states. Note that we refer to the concepts of short- and long-term memory from a behavioral neuroscience point of view: short-term memories of the stimuli are temporary and last for a short amount of time before they fade out, while long-term memory refers to permanently lasting memories of events.[61,62]

Please cite this article in press as: Comoretto et al., Embodying mechano-fluidic memory in soft machines to program behaviors upon interactions, Device (2025), https://doi.org/10.1016/j.device.2025.100863

We develop a long-term memory circuit (Figure 3C) by building upon the circuit with the bistable capacitor in Figure 2G. (1) We add a branch in parallel to the source, connected to the bottom chamber of the memory element, opposite to the actuator. (2) In this new branch, we introduce a normally closed (NC) valve upstream and a venting resistance R_{vent} downstream (22 gauge, 0.5 in). (3) We add a normally open (NO) valve in the actuator branch, between the actuator and the downstream resistance. We can interact with this circuit by closing (and opening) the NO (and NC) valves. To design and test these circuits, we make use of solenoid valves controlled with an input/output electronic board (see the methods), which we will replace in later sections with soft tubes that kink and unkink.[32]

By temporarily closing the NO valve, the actuator line pressurizes (Figure 3D). When the pressure reaches the snap-through pressure of the shell, the shell snaps to the other state, and the capacitor is in the large-volume state. This, in turn, causes the system behavior to operate at low frequency and stroke (after the closing of the NO valve has ended). Then, we can temporarily open the NC valve (Figure 3E), so that the bottom line pressurizes. When the pressure difference between the bottom and top lines reaches the snap-back pressure of the shell, the shell snaps back to the rest state, causing the system behavior to operate at high frequency and stroke. Each time the memory is set to either state via a temporary interaction, the reached state is stable until the next interaction, as a consequence of the bistability of the shell (Figure 3F; Video S2). Therefore, each time a stimulus occurs (opening/closing of NC/NO valves), the system expresses the memory of the past stimulus through its current behavior (frequency and stroke). An LTspice model of this circuit (Figure S8) that treats the bistable capacitor as an assembly of two hysteretic switches that access a fixed capacitance (Note S1) captures this long-term memory effect (Figure S9).

Starting from the design of the long-term memory circuit, we develop a short-term memory circuit (Figure 3G). This circuit is equivalent to the long-term memory circuit, with the only differences being a higher venting resistance (32 gauge, 0.25 in needle), and the shell flipped so that, in the rest state, the chamber connected to the actuator line is in the high-capacitance state (Figure 3G, gray area above the shell). By temporarily opening the NC valve, the pressure in the bottom line increases until the shell snaps, and the system behavior is set to the state with high frequency and stroke (Figure 3H).

After this initial interaction that sets the memory element to the other state, a seemingly counterintuitive behavior occurs, resulting in short-term memory. Given the bistability of the shell, at first, one would expect this system to be bistable as well and, as a consequence, to stabilize at the high state until the next interaction occurs. However, at a system level, two phenomena occur simultaneously after the NC valve has been shortly opened and closed: (1) pressure p_{vent} in the bottom chamber decreases in time as air vents to the atmosphere through the resistance R_{vent} while the valve is closed again (Figures 3I and 3J, yellow); (2) pressure in the top chamber oscillates between ~1 and ~35 kPa, because of the hysteretic valve oscillating. Given these two phenomena, as long as the difference between the bottom and top chamber is greater than the snap-back pressure of the shell (~−10 kPa), the shell stays in the stable snapped branch, because the stability of the shell is determined by the pressure difference between its top and bottom surface (Figure 2E). When the pressure difference between the bottom chamber and the top chamber decreases below ~−10 kPa, the shell snaps back spontaneously, without external interactions (Figure S7 and Video S2). As a consequence, the system self-resets to the low state (Figure 3J, black). Interestingly, the LTspice model (Note S1 and Figure S8) captures how physically flipping the shell in the circuit allows for transitioning from a long-term to a short-term memory response, confirming the spontaneous self-reset (Figure S9).

Note that the snap-back of the shell is not instantaneous, but, instead, it lasts approximately 45 s. This is a consequence of the high venting resistance R_{vent} (32 gauge, 0.25 in needle) limiting airflow. Once the shell initiates the snap-back, it fights against this high venting resistance, effectively compressing the air in the bottom chamber. The signature of this effect, which counters the snap-back of the shell, can be seen in the sudden increase of the pressure p_{vent} in the bottom chamber when the shell initiates the snap-back (Figures S7 and 3J, yellow). During this intermediate phase, the shell is operating in the negative-stiffness regime highlighted with white markers in Figure 2E. When the shell is completely snapped back, at around 90 s in the experiment, p_{vent} finally drops to zero (Figure 3J, rest symbol). Nevertheless, we identify the initiation of the snap-back as the instant when the behavior of the system self-resets to the initial state, because this event is associated with the stroke of the actuator returning to approximately the initial value (Figure 3J, black). Note that since we modeled the bistable shell with ideal hysteretic switches, which do not display the negative-stiffness regime (Note S1), our model (Figure S8) does not capture this intermediate phase between initiation and ending of the snap-back. Rather, the modeled circuit directly snaps back (Figure S9).

The short-term memory circuit temporarily stores information by setting the memory element to the snapped state. After a specific memory-retention time, the system spontaneously self-resets to the rest state (as it was before the interaction occurred) and hence the memory of the occurred stimuli fades away. As confirmed by our LTspice model (Note S1; Figure S8), the memory-retention time can be tuned by selecting different values of venting resistance: higher venting resistance results in slower discharge and, therefore, longer memory-retention time (Figure S9). Within the set of venting resistances that we tested, the memory-retention time ranged from 11 to 71 s (Figure S10).

Fluidic touch sensing via NO and NC kinking tubes

So far, we could interact with the long- and short-term memory circuits through NO and NC solenoid valves, requiring a 24-V signal to close and open the valves (see the methods). With the goal of developing fully fluidic machines that can interact with the surroundings, we aim to develop NO and NC touch sensors harnessing the kinking behavior of soft tubes.[32] We built an NO sensor by bending a commercial elastomeric tube with inner diameter 3 mm, thickness 1 mm, and length 70 mm (Figure 4A). We mechanically compressed the tube to a maximum displacement u_{max} corresponding to the top part of the tube touching the bottom rigid holder. At the same time, we measured the fluidic

Please cite this article in press as: Comoretto et al., Embodying mechano-fluidic memory in soft machines to program behaviors upon interactions, Device (2025), https://doi.org/10.1016/j.device.2025.100863

CellPress
OPEN ACCESS

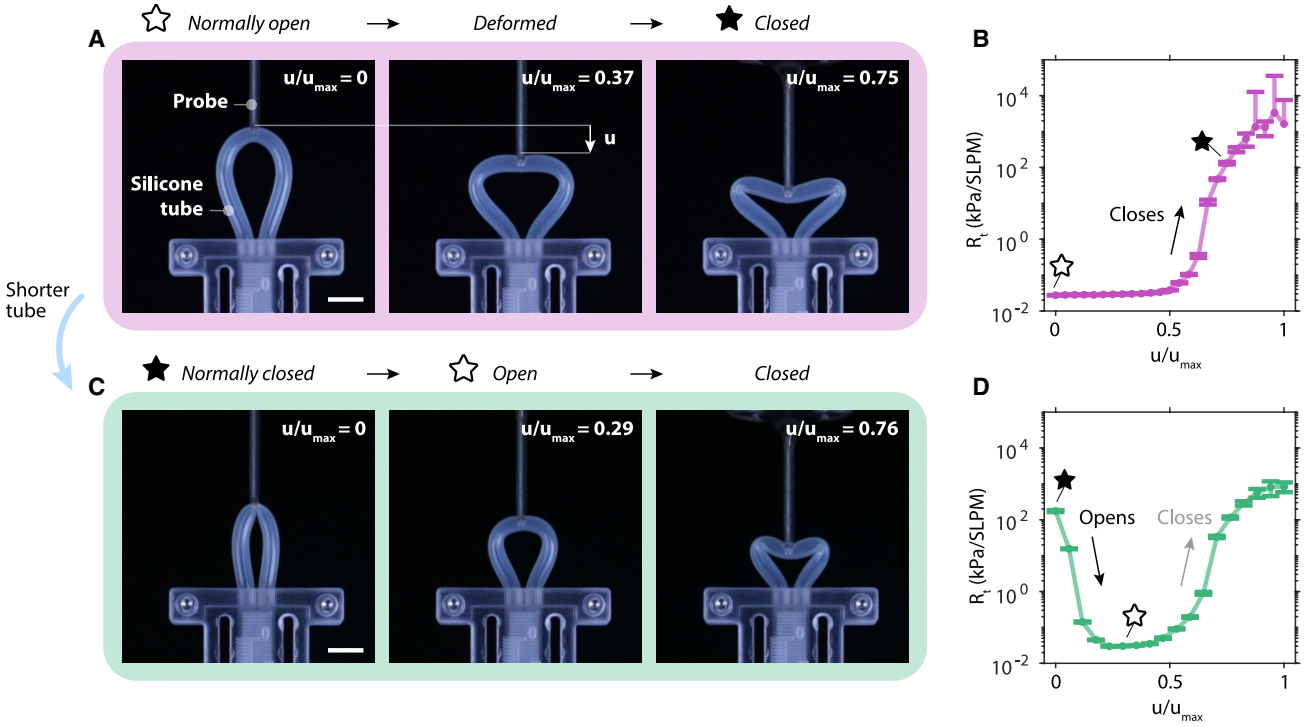

Figure 4. Fluidic touch sensing via NO and NC kinking tubes

(A) A silicone tube (inner diameter 3 mm, thickness 1 mm, and length 70 mm) is bent 180° and constrained at the inlet and outlet in a rigid holder. A probe compresses the tube by moving vertically with a displacement u, first inducing the tube's deformation and then forming two kinks that close the channel.

(B) The fluidic resistance of the tube R_t sharply increases when the two kinks form, indicating the transition from the open state to the closed state.

(C) A shorter tube of length 50 mm displays a kink in its rest state (therefore, it is NC), it unkinks (opens) when compressed, and it forms two kinks when further compressed (it closes again).

(D) The fluidic resistance of the normally closed tube as a function of the probe displacement shows an initial drop (when the tube unkinks, opening) with a subsequent increase (when the two kinks form, closing).

Data in (B) and (D) are reported as mean ± standard deviation. All scale bars represent 1 cm.

resistance of the tube as the ratio between the inlet-outlet pressure difference in kPa and the flow through the tube in standard liters per minute (SLPM). While loading, we observe an initial deformation, followed by a sudden formation of two kinks (Figure 4A). The flow resistance is relatively low ($\sim 1.5 \times 10^{-2}$ kPa SLPM^{-1}) when the tube is not deformed ($u/u_{max} = 0$) (Figure 4B, white star). The resistance stays at approximately the same value until half the maximum probing displacement ($u = 0.5 \cdot u_{max}$). Then, the resistance suddenly increases to $\sim 1 \times 10^{1}$ kPa SLPM^{-1} when $u = 0.6 \cdot u_{max}$. This increase corresponds with the formation of two kinks that block air flow (Figure 4A, black star). The resistance then increases exponentially with increasing probing displacement as the kinks sharpen further. We call this high-resistance state the closed state (Figure 4B, black star) as leakage is limited. So, effectively, the tube is a sensor that transduces information from the mechanical domain (that is, the compressing interaction) into the fluidic domain (that is, the resistance of a fluidic channel).

To build the NC sensor, we found that we can act on a single design parameter of the tube. In fact, by reducing the length of the tube from 70 to 50 mm, a kink spontaneously forms when the tube is not probed (Figure 4C, black star). This is accompanied by the resistance being relatively high ($\sim 1 \times 10^{2}$ kPa SLPM^{-1}) (Figure 4D, black star): the sensor is in an NC state. By compressing, the tube unkinks (Figure 4C, white star), opening the channel, and suddenly decreasing the resistance to $\sim 1.5 \times 10^{-2}$ kPa SLPM^{-1} (Figure 4D, white star). So, the shorter tube is an NC sensor that opens upon interaction. In addition, by further probing the tube after the opening event, it closes again, as two kinks form (Figure 4C).

Therefore, we obtained a touch sensor that, depending on the design parameters, can be in an NO or an NC setting. Interestingly, the NO and NC mechano-fluidic sensors transduce qualitatively equivalent mechanical inputs (compression in one direction) in distinct fluidic information, consisting of closing and opening of channels.

Integration of memory and sensing for programmable behaviors upon user interactions

So far, we have introduced a number of separate ingredients that, when integrated together, we will show can result in programmable behaviors. We have (1) the forward crawling platform (Figure 1); (2) the mechano-fluidic memory element (Figure 2), responsible for providing memory of a stimulus in the form of change in behavior; (3) the short- and long-term memory circuit designs (Figure 3), which read fluidic stimuli in the form of

Please cite this article in press as: Comoretto et al., Embodying mechano-fluidic memory in soft machines to program behaviors upon interactions, Device (2025), https://doi.org/10.1016/j.device.2025.100863

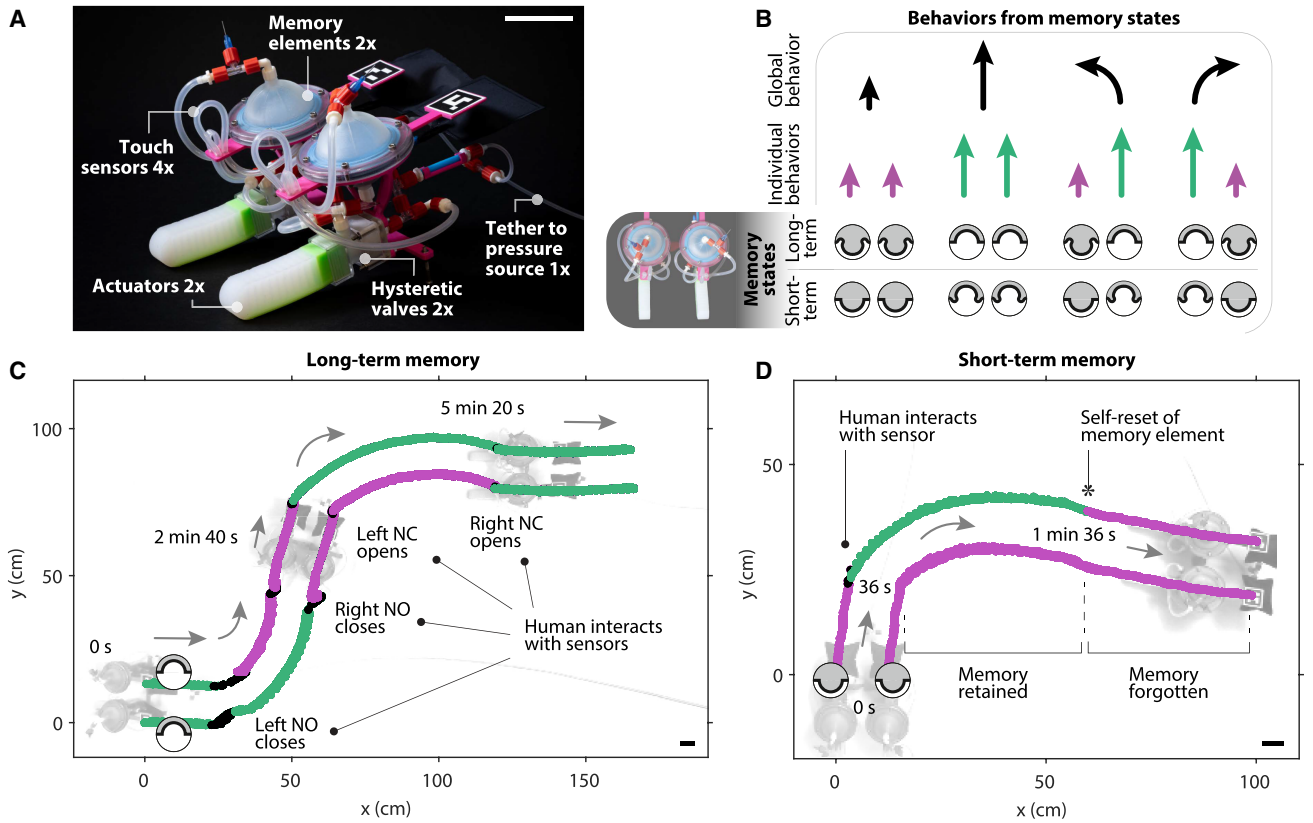

Figure 5. Integration of memory and sensing for programmable behaviors upon user interactions

(A) We build a two-limb machine by mirroring our single-limb platform in Figure 2. The machine is powered by one pressure tether and is equipped with two hysteretic valves, two actuators, two memory units, and four touch sensors (of which two are NO and two NC).

(B) The individual states of the two memory elements impact the individual behavior of the two-halves of the machine, resulting in four different global behaviors of the machine.

(C) With long-term memory settings, the machine locomotes in an arena and switches between steering and forward behaviors when a human operator interacts with the touch sensors by closing the NO and opening the NC sensors.

(D) With short-term memory settings, the machine switches to steering behavior when a human interacts with the sensor, and, after ~1 min, it spontaneously returns to the initial forward-locomoting state.

In (C) and (D), green data points correspond to fast behavior, and purple data points to slow behavior, for each half of the machine. All scale bars represent 5 cm. See also Figure S11 and Video S3.

opening and closing of channels; and (4) the touch sensors (Figure 4), to transduce mechanical stimuli into fluidic ones when a user vertically compresses the tubes.

Now, we integrate these ingredients in a locomoting soft machine that senses external mechanical cues and reacts accordingly (Figure 5A). The machine has two mirrored sides. Each side is built starting from the single-actuator crawling platform, with the memory element and the NO and NC touch sensors placed on top. Internally, the fluidic circuit of each mirrored side is identical to the circuit in Figure 3, while sharing the same pressure source. The two sides of the machine are physically connected with a bearing, to allow rotation (along the mirroring plane) of the two sides relative to each other, as the crawling behavior relies on the rotation induced by the bending actuator (Figure S11). In total, the machine integrates two bending actuators, two hysteretic valves, two memory elements, four touch sensors, and a single tether connected to a pressure source of 1.3 bar.

With two bistable memory elements, the machine has four stable locomoting behaviors (Figure 5B): (1) forward slow, when both individual capacitors are set to the large-volume state; (2) forward fast, when both are set to the small-volume state; (3) steer left, when the right capacitor is set to small-volume state and the left to large-volume state, as the right side of the machine moves at a faster speed compared to the left side, causing global steering; and (4) steer right, when the right capacitor is set to large volume and the left to small.

In Figure 5C, we report the trajectory of the machine locomoting in an arena when receiving touch cues from a human user, with both circuits set to the long-term memory configuration from Figure 3C. The machine starts with both capacitors set to small volume (both shells set to the rest state). Hence, the machine starts locomoting with the fast-forward behavior. Then, the human interacts with the left NO sensor, closing it. After the interaction, the machine steers to the left because the left memory element is set to the large-volume state, and the

Please cite this article in press as: Comoretto et al., Embodying mechano-fluidic memory in soft machines to program behaviors upon interactions, Device (2025), https://doi.org/10.1016/j.device.2025.100863

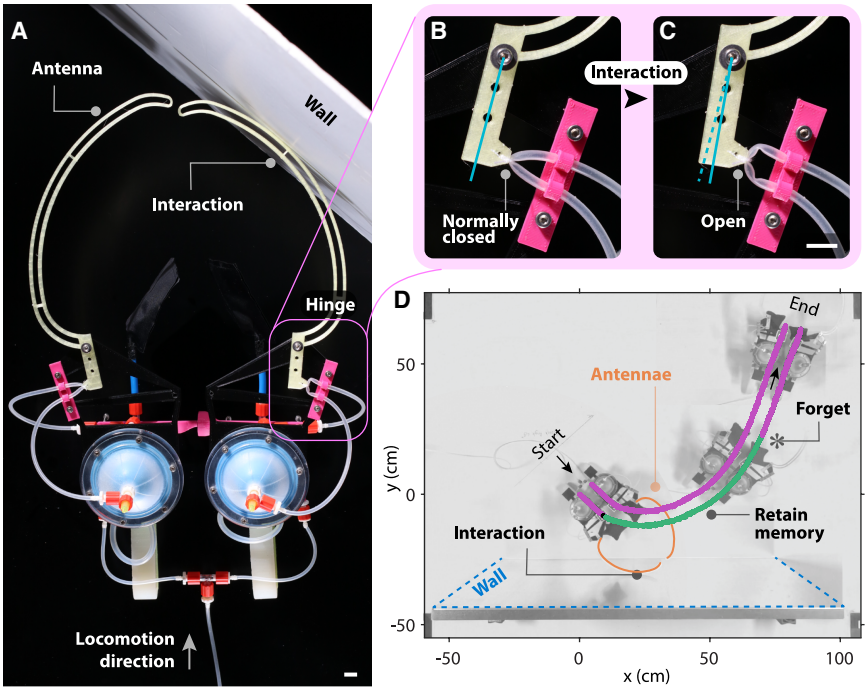

Figure 6. Autonomous obstacle avoidance through short-term memory and insect-inspired sensing

(A) We place two 3D-printed antennae on board the machine, allowing rotation around a hinge upon external interaction with an obstacle, such as a wall.

(B) At the hinge, the antenna is equipped with a kinked tube (with inner diameter 2.5 mm, thickness 0.4 mm, length 30 mm, and distance 10 mm between the inlet and outlet) as an NC sensor.

(C) The tube unkinks upon interaction, effectively sensing the bending moment applied to the antenna and transducing it into fluidic information (drop in fluidic resistance).

(D) The autonomous machine senses the presence of a wall, temporarily retains the memory of the interaction by steering away, and finally forgets the memory of the interaction, going back to the default forward-locomoting behavior. Purple data points indicate slow behavior, and green data points indicate fast behavior, for each half of the machine.

All scale bars represent 1 cm. See also Figure S12 and Video S4.

resulting speed of the left side is lower than the right side. The memory is retained until a new mechanical cue occurs. After the operator closes the right NO sensor by touching it, the machine displays the slow-forward behavior. With the next two interactions, the machine steers to the right and then goes back to the initial fast-forward behavior (Video S3). Additionally, we can interact with two sensors at the same time, closing one and opening the other, to directly switch between sterring left and steering right (Video S3).

When we set the internal circuit to the short-term memory configuration of Figure 3G by flipping the orientation of the memory element and increasing the venting resistance (replacing it with a 34 gauge, 0.25 in needle), the machine also displays short-term memory (Figure 5D). The machine starts with the slow-forward-locomoting behavior. After the user interacts with the left sensor, the left side is set to the high-speed state, and the machine displays the right-steering behavior. After approximately 1 min, the left memory element self-resets to the initial state and the machine spontaneously returns to the forward-locomoting behavior (Video S3). Therefore, the memory of the interaction is retained for approximately 1 min so that the machine steers ~90°. After this amount of time, the memory of the stimulus is forgotten, and the machine goes back to the default behavior, which is moving forward without steering. Short-term memory implies that we can design a preferred behavior, in this case, moving forward, and a temporary behavior, such as steering, that, upon interaction, overrides the default one for a determined amount of time.

Autonomous obstacle avoidance through short-term memory and insect-inspired sensing

So far, the machine was designed for only a specific kind of interaction, where a human user touches the sensor. To demonstrate the potential of integrating memory and sensing for autonomous behaviors, where the machine itself senses the environment without external inputs from a human, we designed an antenna taking inspiration from insects. Often, insects sense the external world with antennae made of relatively rigid flagella and softer pedicel-flagellum junctions (hinges). The hinges are the crucial site for mechanoreception, as they are equipped with dense mechanosensory structures.[63] When the flagellum bends, the receptors in the hinge sense an increase in bending torque, so that the insect detects obstacles[64] or changes in the wind direction.[64,65]

We developed an artificial antenna composed of a rigid 3D-printed flagellum that rotates around a hinge (Figure S12) when it interacts with an external obstacle, such as a wall (Figure 6A). Crucially, when the flagellum rotates, a kinked tube placed at the hinge unkinks (Figures 6B and 6C), acting like the NC touch sensor from Figure 4C. Hence, we localize at the soft hinge the transduction from external mechanical stimuli into internal fluidic information.

We let a machine equipped with two antennae and two short-term memory circuits walk toward a wall with a 45° angle of attack (Figure 6D; Video S4). When the right antenna touches the wall, it rotates around its hinge, unkinking the tube (Figure 6D, label "interaction"). This sensing event results in the memory element snapping to the snapped state, following the same mechanism as previously introduced in Figures 3H. Then, the machine steers away from the wall for approximately 1 min, because the memory of the interaction is retained (Figure 6D, label "retain memory"). After this memory-retention time, the memory element self-resets to the initial state, in the same fashion as explained in Figures 3I and 3J. At this moment in time, the machine forgets the previous interaction with the

Please cite this article in press as: Comoretto et al., Embodying mechano-fluidic memory in soft machines to program behaviors upon interactions, Device (2025), https://doi.org/10.1016/j.device.2025.100863

wall, returning to the forward-locomoting behavior (Figure 6D, label "forget").

DISCUSSION

By embodying mechano-fluidic memory in soft machines, we obtained programmable behaviors upon interaction with the environment without requiring electronics or software for control. We introduced memory in a soft, self-oscillating crawler through the bistability of a physical parameter of the machine, the capacitance, by leveraging a bistable elastic shell. With long- and short-term memory circuits and kinking tubes as touch sensors, the machine could detect interactions with a user and obstacles, and consequently switch behavior between walking straight and steering.

We instilled memory and feedback by selectively coupling together a low number of components (shells and tubes) that display highly nonlinear behavior. This approach parts ways from general-purpose robotics, which instead typically relies on a large number of relatively simple components in a central computer, in the range of billions of nanoscale transistors.[66] We envision that this approach of integrating a limited number of nonlinear components will prove effective for task-specific applications[67] where specialized tasks are prespecified and robustness is of the essence, as it reduces the overall design complexity in terms of number of components.

For instance, in biomedical applications, microrobots could autonomously navigate inside the human body[68] and detect cancer tissues by sensing a difference in stiffness[69,70] without carrying microelectronics.[71] We also foresee using these mechanical effects as "reflexes" embedded in the structure of machines, to which some tasks can be offloaded from a central controller. For example, in space applications, robots could delegate the autonomous exploration task to their mechanical body, preventing the breakdown of the locomoting apparatus in case of solar storm events.[72] For environmental monitoring applications,[73] self-oscillating machines could autonomously crawl or swim by harnessing their responsive bodies. By removing the need for electronics carried on board, the machines could potentially be constructed monolithically[36,47] with biodegradable materials. By deploying a large number of biodegradable, simple, yet robust machines[74] with basic capabilities of sensing and memory, instead of a few general-purpose and relatively complex robots, we envision monitoring remote areas with minimal impact on the surrounding environment. To close the gap between our current exploratory work (focused on the principles of embodied memory) and these real-world applications, further research is required, especially around the topics of energy efficiency and scalability.

Even though our work mainly focused on conceptually demonstrating a way to introduce fluidic circuits with memory and sensing, it is important to note that, from a practical perspective, our current implementation of the machines as assemblies of various custom-made parts carries the main downside of limited reliability for real-world applications. For instance, the hysteretic valves have a limited lifetime, as the elastomer degrades around the slits after ~100,000 cycles, leading to a change in frequency.[37] The pouch capacitors tend to rupture around the corners after prolonged use (on the order of tens of hours), likely due to stress concentrations. Moreover, the two-actuator locomoting machine intrinsically relies on symmetry between the two halves to avoid drifting while crawling straight. To achieve symmetric behavior, we had to manufacture a relatively large number of samples for each component and select pairs that behaved similarly. For these reasons, in future work, we will focus on more robust manufacturing approaches. For instance, using fluidic oscillators that do not require cutting silicone, such as those that use magnets,[75] could improve the machines' lifetime. Moreover, we envision that developing components where multiple functionalities coexist, such as actuators that also self-oscillate,[19] will increase the machines' simplicity and, consequently, their reliability.

Our proposed approach will particularly benefit from carefully tuning the interactions,[76] both internal to the machines and with the external environment. However, this potential will come with the associated downside of an increased complexity of the design process that takes into account the interactions. While here we specifically focused on memory, other complex behaviors are within reach through mechanical interactions, as demonstrated by initial results on self-learning mechanical circuits[77] and many-agent cooperation through implicit mechanical couplings.[78] This "integrative mechanics" approach is the artificial parallel to integrative biology, where complex dynamic behaviors emerge from the interplay between interactions within the agent and with the environment in which the agent is situated. These specialized, distributed, and redundant interactions found in biological systems enable high levels of robustness, while not sacrificing functionality: autonomous machines have the potential to tap into this vast complexity as well, with embodied memory being one step further in this direction.

METHODS

Design and manufacturing

Hysteretic valves, bending actuators, soft resistors, and inextensible capacitors

The design and the manufacturing procedure of the hysteretic valves are based on the original design we previously introduced.[37] We scaled up the original design by a factor of 2 in all dimensions, and we introduced a notch in the rigid holders in the same way as described in detail in our previous work.[43]

The bending PneuNet actuator was previously reproduced by our lab, and both its design and the manufacturing steps are described in detail in our previous work.[48,53] The actuator presents two sides, manufactured via two consecutive injection-molding steps. The inflating side with hollow chambers is made of DragonSkin 10 (DS10) silicone (Smooth-On). The stiffer side is made of Elite Double 32 (ED32) silicone (Zhermack) with an embedded inextensible grid fabric (Penelope 70/10, Garenenzo). Before injecting ED32, it is essential to wait for DS10 to be partially cured (3.5 h of the total 5-h curing time), to allow for stronger bonding between the two silicones.

The soft resistors, implemented as pre-resistances in all the circuits, are elastomeric hollow cylinders made of Smooth-Sil 950 (Smooth-On), with outer diameter 5 mm, inner diameter

Please cite this article in press as: Comoretto et al., Embodying mechano-fluidic memory in soft machines to program behaviors upon interactions, Device (2025), https://doi.org/10.1016/j.device.2025.100863

0.35 mm, and length 40 mm. The soft resistors are manufactured via injection molding, with a two-part outer mold and a metal rod with diameter 0.35 mm as the inner mold.

The inextensible capacitors are made of two TPU-coated nylon sheets (nylon 70den TPU-coated one side 170g/m^2 heat-sealable, extremtextil) that we heat-seal along a specified path. The path is a rectangle, with an opening on one of the short sides (Figure S13). Given the width w and the height h, we calculate the geometric volume V of the pouch when inflated as the solution to the paper-bag problem[79]:

$$V = w^3 \cdot \left(\frac{h}{\pi w} - 0.142 \cdot \left(1 - 10^{-h/w} \right) \right). \quad \text{(Equation 1)}$$

The two sheets are heat-sealed using the 3D printer Felix Tec 4. The printer presents a custom-made hot head, previously used by our group,[19,52] that consists of a spherical hot nozzle and a spring that ensures even sealing lines. A silicone mat is placed between the printer bed and the sheets, and oven paper is placed on top of the sheets. To the printer, we send a G-code based on an Adobe Illustrator file containing the desired tool path. After sealing, we cut the residual material surrounding the sealing lines and, in the open side of the pouch, we heat-seal the sheets to a TPU Festo tube with a soldering iron at 300°. Finally, we place Luer connectors (MLRL007-1 Male Luer to 500 Series Barb 3/32″ 2.4 mm with Lock Ring FSLLR-3) in the Festo tubes.

Throughout the article, we place a fixed pre-capacitor with volume $V_{pre} = 60$ mL (with $w = h = 68$ mm) on the machines (except in Figures S4A–S4C, where we purposefully vary the pre-capacitance).

Bistable shells

The bistable shells are defined by four parameters, as illustrated in Figure S5A: the thickness t, the angle α from the vertical axis, the base width w, and the boundary radius R_b. Throughout our study, the shells have $t = 3$ mm, $\alpha = 80°$, $w = 55$ mm, and $R_b = 2.28$ mm. In addition, the shells have an outer notch and a rim that allow for centering when being mounted in the rigid holders. The rigid holder clamps the shell along the outer rim, held together with screws (Figure S5B). The rigid holders compress the silicone rim of 0.95 mm ($\sim$ 30% of its thickness).

The shells are manufactured via injection molding of Smooth-Sil 950 silicone (Smooth-On) using a two-part outer mold. The outer molds were printed in VeroClear (Stratasys) with a PolyJet 3D printer (Eden260VS, Stratasys). Before molding, we sprayed a thin layer of release agent (Ease release 200, Smooth-On) on the inner surface of the molds to ease demolding after curing.

Crawling soft machines

The single-actuator crawling soft machine reported in Figure 1 consists of various individual components (Figure S11). The first component consists of two rigid 3D-printed parts that hold the hysteretic valve in place. The part on the outlet side of the valve has a cavity where the bending actuator is press-fitted. Both inlet and outlet parts have a hole with diameter 5.5 mm, which, after tapping with a 1/4–28 Unified National Fine (UNF) tap, allows for the insertion of a threaded Luer connector (Luer quick-turn tube coupling 1/4-28 UNF). These Luer connectors allow for the other modules (heat-sealed pouches, resistors, and shells) to be quickly connected. In addition, on the inlet side, we attach a 3D-printed adapter, on which we place screws that act as rigid legs of height 25 mm.

The two-actuator crawling soft machine (Figure 5) consists of two mirrored copies of the single-actuator crawler. The only difference lies in the adapter for the rigid legs, which is designed to accommodate a bearing (Figure S11). The bearing allows for the rotation (along the mirroring plane) of the two single-actuator sides with respect to each other, decoupling the two rotational degrees of freedom. In this way, when the two actuators activate at different frequencies and amplitudes, the two sides locomote at different speeds. Without the bearing, when one side actuates, the other side would drag along.

Experimental setups

Measuring fluidic quantities

To regulate and measure the fluidic quantities of interest (pressure and flow), we use a custom-made acquisition setup previously used by our group.[19,37,43,48] The setup is based on the National Instruments IN USB-6212 input/output board, with software developed in house. A proportional pressure regulator (Festo VEAB-L-26-D18-Q4-V1-1R1) is controlled using an analog port of the board. The regulator is connected to an upstream precision pressure regulator (Festo LRP-1/4–10), connected to the building pressure source. The setup has various analog input ports, which read the voltage from the pressure sensors (NXP MPX4250DP) and flow sensors (Honeywell AWM5101VN, Honeywell AWM5104VN). The fluidic connection between the parts (regulators, valves, sensors, and samples) is implemented with silicone tubes (Rubbermagazijn 2 $\times$ 4 mm and 3 $\times$ 6 mm), Festo tubes (PUN-6X1-BL), and Luer connectors (male-female, Luer-to-barb, and T connectors).

In the benchtop fluidic experiments in Figures 1H, 1I, 3, S4A, S4B, S4D, S4E, and S10A, the soft machine is held in place with the actuator not interacting with the ground, free to bend in mid-air. Detecting an ArUco marker placed at the tip of the actuator allows for determining the vertical stroke of the actuator when it does not interact with the ground. The NC and NO 24 V solenoid valves (SMC Solenoid Valve VDW250-5G-2-01F-Q) used in the benchtop experiments are controlled through digital output ports of the input/output board.

Compressing the fluidic touch sensors

To measure the fluidic resistance of the kinking tubes as a function of their deformation (Figure 4), we make use of a fluidic analog of a resistive voltage divider circuit. Using the fluidic-electrical analogy,[37,50] we treat pressure as voltage. The kinking tube is placed in series with a resistor (a needle) that vents to atmosphere. This resistor has a fixed known resistance $R_0 \approx$ 0.5 kPa SLPM^{-1} that we measured separately as the slope of the characteristic pressure-flow curve of the needle. We then connect the kinking tube to a pressure regulator upstream (1.5 bar), and we measure the pressure before the kinking tube p_{in} and the pressure after the kinking tube p_{out}, from which we can derive the resistance of the kinking tube R_t:

$$R_t = R_0 \cdot \left(\frac{p_{in}}{p_{out}} - 1 \right). \quad \text{(Equation 2)}$$

The pressure data are acquired for various static deformation states of the tube. The tube is deformed in increments of 1 mm using a rigid probe, controlled with a tensile-testing machine Instron 5965. The starting moment of each Instron compression is triggered by a digital output signal from the fluidic setup, ensuring that the acquisitions in both setups are synchronized. In Figure 4, each datapoint is the average fluidic resistance (with standard deviation) over 5 s of this static compression condition.

Obtaining the pressure-volume curves

To obtain the pressure-volume curves of the capacitors in Figures 2 and S6, we quasi-statically inject a controlled amount of water into the capacitors. We mechanically connect a syringe to the tensile-testing Instron 5965 machine, and we fluidically connect it to the capacitors making sure all air bubbles are removed. We ramp the displacement of the tensile-testing machine at a rate of 100 mm min^{-1}. Since water is incompressible, controlling the displacement of the syringe means controlling the geometric volume provided to the capacitors. Knowing the diameter of the syringe 26.4 mm, volume is therefore ramped at a rate of 54.74 mL min^{-1}. While controlling volume, we measure pressure inside the capacitors with a water-compatible pressure sensor (Honeywell 6DF5G). Since the injected water has substantial mass, to remove the effect of gravity on the pressure-volume curves, we submerge the capacitors in a water tank while performing the tests.

Tracking machines' location

To extrapolate the location of the locomoting machines, we place ArUco markers on board the machines, and we use the Python library OpenCV to detect the ArUcos for each frame of the GoPro videos. We first convert each frame to grayscale using the command cv2.cvtColor. We then correct for warp and distortion of the GoPro camera, using four static ArUco markers placed as a reference at the corners of the canvas, with the command cv2.warpPerspective. Then, we detect the ArUcos with the command cv2.aruco.detectMarkers.

LTspice model

Domain analogies

Using the fluidic-electronic analogy,[37,50] we model the fluidic system using both constant and variable linear resistors, linearized capacitors, and hysteretic voltage-controlled switches to qualitatively capture the experimentally observed behaviors. The theory behind domain analogies treats pressure as voltage and flow as current, allowing us to model the fluidic circuits as equivalent electronic circuits using the LTspice software (Analog Devices). See Note S1 for a description of the assumptions that allow this equivalence to hold and for the following derivation of the models of each component.

Modeling the individual components and the circuits

In summary, we model the fluidic resistor R as the coefficient of the linear relation between the pressure drop p across the resistor and the flow rate Q through the resistor as $p = R \cdot Q$. Using the fluidic-electrical analogy, in LTspice, the resistor R is governed by Ohm's law, relating voltage drop V and current I as $V = R \cdot I$.

We model the fluidic capacitor as an element that relates pressure p to volume V. In its linearized form, we have

$$V = C \cdot p, \qquad \text{(Equation 3)}$$

with C the total capacitance. Crucially, in Note S1, we report a formulation of the total pneumatic capacitance as the sum of two contributions[51]:

$$C = \frac{V}{K} + \frac{\partial V}{\partial p}, \qquad \text{(Equation 4)}$$

with K the bulk modulus of the gas. Hence, the total pneumatic capacitance has contributions from (1) the change in density due to pressure by compressibility of the gas and (2) the change in volume due to pressure by elasticity of the container. Taking the time derivative on both sides of Equation 3, it can be rewritten as a proportional relationship between the volumetric flow rate Q and the rate of pressure change $\frac{dp}{dt}$ as $Q = C\frac{dp}{dt}$, which in the electrical domain corresponds to $I = C\frac{dV}{dt}$.

As in our previous work,[37] we model the hysteretic valve as a voltage-controlled hysteretic switch that opens at a critical voltage that is higher than the closing voltage. Lastly, we model the bistable capacitor as an assembly of two coupled voltage-controlled hysteretic switches that access a fixed capacitance.

In Figures S2 and S8, we report the schematics of the LTspice models of the circuits of Figures 1 and 3, respectively. In Figures S3 and S9, we report the results of the simulations compared to the experiments.

RESOURCE AVAILABILITY

Lead contact

Requests for further information and resources should be directed to and will be fulfilled by the lead contact, Johannes T.B. Overvelde (b.overvelde@amolf.nl).

Materials availability

This study did not generate new materials.

Data and code availability

- All original data, code, and manufacturing resources have been deposited at Zenodo and are publicly available as of the date of publication at DOI: https://doi.org/10.5281/zenodo.14621970.
- Any additional information required to reanalyze the data reported in this paper is available from the lead contact upon request.

ACKNOWLEDGMENTS

We thank all members of our Soft Robotic Matter Group for the invaluable discussions. We thank Niels Commandeur for technical support. J.T.B.O. acknowledges the European Union's 2020 ERC-STG under grant agreement no. 948132. This work is part of the Dutch Research Council (NWO) and was performed at the research institute AMOLF. This work is part of the Holland Hybrid Heart project, financed by the Hartstichting and the Dutch Research Council (NWO) with file number NWA.1518.22.049 of the research program NWA L1 - Onderzoek op Routes door Consortia 2022 - NWA-ORC 2022.

AUTHOR CONTRIBUTIONS

Conceptualization, A.C. and J.T.B.O.; methodology, A.C., S.K., and J.T.B.O.; software, A.C.; formal analysis, A.C., S.K., and J.T.B.O.; investigation, A.C. and T.M.; writing – original draft, A.C. and J.T.B.O.; writing – review & editing,

A.C., S.K., and J.T.B.O.; visualization, A.C.; funding acquisition, J.T.B.O.; supervision, J.T.B.O.

DECLARATION OF INTERESTS

The authors declare no competing interests.

SUPPLEMENTAL INFORMATION

Supplemental information can be found online at https://doi.org/10.1016/j.device.2025.100863.

Received: March 3, 2025
Revised: June 16, 2025
Accepted: June 22, 2025

REFERENCES

1. Rus, D., and Tolley, M.T. (2015). Design, fabrication and control of soft robots. Nature *521*, 467–475. https://doi.org/10.1038/nature14543.
2. Kim, S., Laschi, C., and Trimmer, B. (2013). Soft robotics: a bioinspired evolution in robotics. Trends Biotechnol. *31*, 287–294. https://doi.org/10.1016/j.tibtech.2013.03.002.
3. Whitesides, G.M. (2018). Soft robotics. Angew. Chem. Int. Ed. Engl. *57*, 4258–4273. https://doi.org/10.1002/anie.201800907. https://onlinelibrary.wiley.com/doi/abs/10.1002/anie.201800907. https://onlinelibrary.wiley.com/doi/pdf/10.1002/anie.201800907.
4. Pfeifer, R., and Bongard, J. (2006). How the Body Shapes the Way We Think: A New View of Intelligence (The MIT Press). https://doi.org/10.7551/mitpress/3585.001.0001.
5. Brown, E., Rodenberg, N., Amend, J., Mozeika, A., Steltz, E., Zakin, M.R., Lipson, H., and Jaeger, H.M. (2010). Universal robotic gripper based on the jamming of granular material. Proc. Natl. Acad. Sci. USA *107*, 18809–18814. https://doi.org/10.1073/pnas.1003250107. https://www.pnas.org/doi/abs/10.1073/pnas.1003250107. https://www.pnas.org/doi/pdf/10.1073/pnas.1003250107.
6. Drotman, D., Jadhav, S., Karimi, M., de Zonia, P., and Tolley, M.T. (2017). 3d printed soft actuators for a legged robot capable of navigating unstructured terrain. In 2017 IEEE International Conference on Robotics and Automation (ICRA), pp. 5532–5538. https://doi.org/10.1109/ICRA.2017.7989652.
7. Tolley, M.T., Shepherd, R.F., Mosadegh, B., Galloway, K.C., Wehner, M., Karpelson, M., Wood, R.J., and Whitesides, G.M. (2014). A resilient, untethered soft robot. Soft Robot. *1*, 213–223. https://doi.org/10.1089/soro.2014.0008.
8. Conrad, S., Teichmann, J., Auth, P., Knorr, N., Ulrich, K., Bellin, D., Speck, T., and Tauber, F.J. (2024). 3d-printed digital pneumatic logic for the control of soft robotic actuators. Sci. Robot. *9*, eadh4060. https://doi.org/10.1126/scirobotics.adh4060. https://www.science.org/doi/abs/10.1126/scirobotics.adh4060. https://www.science.org/doi/pdf/10.1126/scirobotics.adh4060.
9. Bai, H., Kim, Y.S., and Shepherd, R.F. (2022). Autonomous self-healing optical sensors for damage intelligent soft-bodied systems. Sci. Adv. *8*, eabq2104. https://doi.org/10.1126/sciadv.abq2104. https://www.science.org/doi/abs/10.1126/sciadv.abq2104. https://www.science.org/doi/pdf/10.1126/sciadv.abq2104.
10. Heydari, S., Johnson, A., Ellers, O., McHenry, M.J., and Kanso, E. (2020). Sea star inspired crawling and bouncing. J. R. Soc. Interface *17*, 20190700, arXiv: https://royalsocietypublishing.org/doi/pdf/10.1098/rsif.2019.0700. https://doi.org/10.1098/rsif.2019.0700. https://royalsocietypublishing.org/doi/abs/10.1098/rsif.2019.0700.
11. Po, T., Kanso, E., and McHenry, M.J. (2024). Cooperative transport in sea star locomotion. Curr. Biol. *34*, 2551–2557.e4. https://doi.org/10.1016/j.cub.2024.03.042. https://www.sciencedirect.com/science/article/pii/S0960982224003828.
12. Delvolvé, I., Bem, T., and Cabelguen, J.M. (1997). Epaxial and limb muscle activity during swimming and terrestrial stepping in the adult newt, pleurodeles waltl. J. Neurophysiol. *78*, 638–650. https://doi.org/10.1152/jn.1997.78.2.638.
13. Ijspeert, A.J., Crespi, A., Ryczko, D., and Cabelguen, J.M. (2007). From swimming to walking with a salamander robot driven by a spinal cord model. Science *315*, 1416–1420. https://doi.org/10.1126/science.1138353. https://www.science.org/doi/abs/10.1126/science.1138353. https://www.science.org/doi/pdf/10.1126/science.1138353.
14. Flavell, S.W., Raizen, D.M., and You, Y.J. (2020). Behavioral States. Genetics *216*, 315–332. https://doi.org/10.1534/genetics.120.303539. https://academic.oup.com/genetics/article-pdf/216/2/315/38862116/genetics0315.pdf.
15. Kamp, L.M., Zanaty, M., Zareei, A., Gorissen, B., Wood, R.J., and Bertoldi, K. (2024). Reprogrammable sequencing for physically intelligent underactuated robots. ArXiv. https://doi.org/10.48550/arXiv.2409.03737.
16. Zhao, Y., Chi, Y., Hong, Y., Li, Y., Yang, S., and Yin, J. (2022). Twisting for soft intelligent autonomous robot in unstructured environments. Proc. Natl. Acad. Sci. USA *119*, e2200265119. https://doi.org/10.1073/pnas.2200265119. https://www.pnas.org/doi/abs/10.1073/pnas.2200265119. https://www.pnas.org/doi/pdf/10.1073/pnas.2200265119.
17. Xi, Y., Marzin, T., Huang, R.B., Jones, T.J., and Brun, P.T. (2024). Emergent behaviors of buckling-driven elasto-active structures. Proc. Natl. Acad. Sci. USA *121*, e2410654121. https://doi.org/10.1073/pnas.2410654121. https://www.pnas.org/doi/abs/10.1073/pnas.2410654121. https://www.pnas.org/doi/pdf/10.1073/pnas.2410654121.
18. He, Q., Yin, R., Hua, Y., Jiao, W., Mo, C., Shu, H., and Raney, J.R. (2023). A modular strategy for distributed, embodied control of electronics-free soft robots. Sci. Adv. *9*, eade9247. https://doi.org/10.1126/sciadv.ade9247. https://www.science.org/doi/abs/10.1126/sciadv.ade9247. https://www.science.org/doi/pdf/10.1126/sciadv.ade9247.
19. Comoretto, A., Schomaker, H.A.H., and Overvelde, J.T.B. (2025). Physical synchronization of soft self-oscillating limbs for fast and autonomous locomotion. Science *388*, 610–615. https://doi.org/10.1126/science.adr3661. https://www.science.org/doi/abs/10.1126/science.adr3661.
20. Kaspar, C., Ravoo, B.J., van der Wiel, W.G., Wegner, S.V., and Pernice, W.H.P. (2021). The rise of intelligent matter. Nature *594*, 345–355.
21. Chen, T., Pauly, M., and Reis, P.M. (2021). A reprogrammable mechanical metamaterial with stable memory. Nature *589*, 386–390. https://doi.org/10.1038/s41586-020-03123-5.
22. Yasuda, H., Buskohl, P.R., Gillman, A., Murphey, T.D., Stepney, S., Vaia, R.A., and Raney, J.R. (2021). Mechanical computing. Nature *598*, 39–48.
23. Kwakernaak, L.J., and van Hecke, M. (2023). Counting and sequential information processing in mechanical metamaterials. Phys. Rev. Lett. *130*, 268204. https://doi.org/10.1103/PhysRevLett.130.268204. https://link.aps.org/doi/10.1103/PhysRevLett.130.268204.
24. Jules, T., Reid, A., Daniels, K.E., Mungan, M., and Lechenault, F. (2022). Delicate memory structure of origami switches. Phys. Rev. Res. *4*, 013128.
25. Bense, H., and van Hecke, M. (2021). Complex pathways and memory in compressed corrugated sheets. Proc. Natl. Acad. Sci. USA *118*, e2111436118, arXiv:https://www.pnas.org/doi/pdf/10.1073/pnas.2111436118. https://doi.org/10.1073/pnas.2111436118. https://www.pnas.org/doi/abs/10.1073/pnas.2111436118.
26. Shohat, D., Hexner, D., and Lahini, Y. (2022). Memory from coupled instabilities in unfolded crumpled sheets. Proc. Natl. Acad. Sci. USA *119*, e2200028119. https://doi.org/10.1073/pnas.2200028119. https://www.pnas.org/doi/abs/10.1073/pnas.2200028119. https://www.pnas.org/doi/pdf/10.1073/pnas.2200028119.
27. Guo, X., Guzmán, M., Carpentier, D., Bartolo, D., and Coulais, C. (2023). Non-orientable order and non-commutative response in frustrated metamaterials. Nature *618*, 506–512.

28. Yasuda, H., Tachi, T., Lee, M., and Yang, J. (2017). Origami-based tunable truss structures for non-volatile mechanical memory operation. Nat. Commun. *8*, 962.

29. McDonald, K., and Ranzani, T. (2021). Hardware methods for onboard control of fluidically actuated soft robots. Front. Robot. AI *8*, 720702. https://doi.org/10.3389/frobt.2021.720702. https://www.frontiersin.org/articles/10.3389/frobt.2021.720702.

30. Vasios, N., Gross, A.J., Soifer, S., Overvelde, J.T.B., and Bertoldi, K. (2020). Harnessing viscous flow to simplify the actuation of fluidic soft robots. Soft Robot. *7*, 1–9. https://doi.org/10.1089/soro.2018.0149.

31. Matia, Y., Kaiser, G.H., Shepherd, R.F., Gat, A.D., Lazarus, N., and Petersen, K.H. (2023). Harnessing nonuniform pressure distributions in soft robotic actuators. Advanced Intelligent Systems *5*, 2200330. https://doi.org/10.1002/aisy.202200330. https://onlinelibrary.wiley.com/doi/abs/10.1002/aisy.202200330. https://onlinelibrary.wiley.com/doi/pdf/10.1002/aisy.202200330.

32. Luo, K., Rothemund, P., Whitesides, G.M., and Suo, Z. (2019). Soft kink valves. J. Mech. Phys. Solid. *131*, 230–239. https://doi.org/10.1016/j.jmps.2019.07.008. https://www.sciencedirect.com/science/article/pii/S0022509619303473.

33. Overvelde, J.T.B., Kloek, T., D'haen, J.J.A., and Bertoldi, K. (2015). Amplifying the response of soft actuators by harnessing snap-through instabilities. Proc. Natl. Acad. Sci. USA *112*, 10863–10868. https://doi.org/10.1073/pnas.1504947112. https://www.pnas.org/doi/abs/10.1073/pnas.1504947112. https://www.pnas.org/doi/pdf/10.1073/pnas.1504947112.

34. Decker, C.J., Jiang, H.J., Nemitz, M.P., Root, S.E., Rajappan, A., Alvarez, J.T., Tracz, J., Wille, L., Preston, D.J., and Whitesides, G.M. (2022). Programmable soft valves for digital and analog control. Proc. Natl. Acad. Sci. USA *119*, e2205922119. https://doi.org/10.1073/pnas.2205922119. https://www.pnas.org/doi/abs/10.1073/pnas.2205922119. https://www.pnas.org/doi/pdf/10.1073/pnas.2205922119.

35. Rothemund, P., Ainla, A., Belding, L., Preston, D.J., Kurihara, S., Suo, Z., and Whitesides, G.M. (2018). A soft, bistable valve for autonomous control of soft actuators. Sci. Robot. *3*, eaar7986. https://doi.org/10.1126/scirobotics.aar7986. https://www.science.org/doi/abs/10.1126/scirobotics.aar7986. https://www.science.org/doi/pdf/10.1126/scirobotics.aar7986.

36. Zhai, Y., Boer, A.D., Yan, J., Shih, B., Faber, M., Speros, J., Gupta, R., and Tolley, M.T. (2023). Desktop fabrication of monolithic soft robotic devices with embedded fluidic control circuits. Sci. Robot. *8*, eadg3792. https://doi.org/10.1126/scirobotics.adg3792. https://www.science.org/doi/abs/10.1126/scirobotics.adg3792. https://www.science.org/doi/pdf/10.1126/scirobotics.adg3792.

37. van Laake, L.C., de Vries, J., Malek Kani, S., and Overvelde, J.T.B. (2022). A fluidic relaxation oscillator for reprogrammable sequential actuation in soft robots. Matter *5*, 2898–2917. https://doi.org/10.1016/j.matt.2022.06.002. https://www.sciencedirect.com/science/article/pii/S2590238522002971.

38. Mousa, M., Rezanejad, A., Gorissen, B., and Forte, A.E. (2024). Frequency-controlled fluidic oscillators for soft robots. Adv. Sci. (Weinh). *11*, 2470264. https://doi.org/10.1002/advs.202470264. https://onlinelibrary.wiley.com/doi/abs/10.1002/advs.202470264. https://onlinelibrary.wiley.com/doi/pdf/10.1002/advs.202470264.

39. Gorissen, B., Milana, E., Baeyens, A., Broeders, E., Christiaens, J., Collin, K., Reynaerts, D., and De Volder, M. (2019). Hardware sequencing of inflatable nonlinear actuators for autonomous soft robots. Adv. Mater. *31*, 1804598. https://onlinelibrary.wiley.com/doi/abs/10.1002/adma.201804598 10.1002/adma.201804598. https://onlinelibrary.wiley.com/doi/pdf/10.1002/adma.201804598.

40. Van Raemdonck, B., Milana, E., De Volder, M., Reynaerts, D., and Gorissen, B. (2023). Nonlinear inflatable actuators for distributed control in soft robots. Adv. Mater. *35*, 2301487, arXiv:https://advanced.onlinelibrary.wiley.com/doi/pdf/10.1002/adma.202301487. https://doi.org/10.1002/adma.202301487. https://advanced.onlinelibrary.wiley.com/doi/abs/10.1002/adma.

41. Preston, D.J., Rothemund, P., Jiang, H.J., Nemitz, M.P., Rawson, J., Suo, Z., and Whitesides, G.M. (2019). Digital logic for soft devices. Proc. Natl. Acad. Sci. USA *116*, 7750–7759. https://doi.org/10.1073/pnas.1820672116. https://www.pnas.org/doi/abs/10.1073/pnas.1820672116. https://www.pnas.org/doi/pdf/10.1073/pnas.1820672116.

42. Lee, W.K., Preston, D.J., Nemitz, M.P., Nagarkar, A., MacKeith, A.K., Gorissen, B., Vasios, N., Sanchez, V., Bertoldi, K., Mahadevan, L., and Whitesides, G.M. (2022). A buckling-sheet ring oscillator for electronics-free, multimodal locomotion. Sci. Robot. *7*, eabg5812. https://doi.org/10.1126/scirobotics.abg5812. https://www.science.org/doi/abs/10.1126/scirobotics.abg5812. https://www.science.org/doi/pdf/10.1126/scirobotics.abg5812.

43. van Laake, L.C., Comoretto, A., and Overvelde, J.T.B. (2024). On the coexistence of pressure regulation and oscillation modes in soft hysteretic valves. J. Fluid Struct. *126*, 104090. https://doi.org/10.1016/j.jfluidstructs.2024.104090. https://www.sciencedirect.com/science/article/pii/S0889974624000252.

44. Wehner, M., Truby, R.L., Fitzgerald, D.J., Mosadegh, B., Whitesides, G.M., Lewis, J.A., and Wood, R.J. (2016). An integrated design and fabrication strategy for entirely soft, autonomous robots. Nature *536*, 451–455. https://doi.org/10.1038/nature19100.

45. Drotman, D., Jadhav, S., Sharp, D., Chan, C., and Tolley, M.T. (2021). Electronics-free pneumatic circuits for controlling soft-legged robots. Sci. Robot. *6*, eaay2627. https://doi.org/10.1126/scirobotics.aay2627. https://www.science.org/doi/abs/10.1126/scirobotics.aay2627. https://www.science.org/doi/pdf/10.1126/scirobotics.aay2627.

46. Tanaka, S., Nabae, H., and Suzumori, K. (2024). Serially coupled self-excited pneumatic actuator for environment-adaptive steering robot. IEEE Robot. Autom. Lett. *9*, 10479–10486. https://doi.org/10.1109/LRA.2024.3475048.

47. Zhai, Y., Yan, J., De Boer, A., Faber, M., Gupta, R., and Tolley, M.T. (2025). Monolithic desktop digital fabrication of autonomous walking robots. Advanced Intelligent Systems *7*, 2400876.

48. Picella, S., van Riet, C.M., and Overvelde, J.T.B. (2024). Pneumatic coding blocks enable programmability of electronics-free fluidic soft robots. Sci. Adv. *10*, eadr2433. https://doi.org/10.1126/sciadv.adr2433. https://www.science.org/doi/abs/10.1126/sciadv.adr2433. https://www.science.org/doi/pdf/10.1126/sciadv.adr2433.

49. Taffetani, M., Jiang, X., Holmes, D.P., and Vella, D. (2018). Static bistability of spherical Caps. Proc. Math. Phys. Eng. Sci. *474*, 20170910. https://doi.org/10.1098/rspa.2017.0910.

50. Oh, K.W., Lee, K., Ahn, B., and Furlani, E.P. (2012). Design of pressure-driven microfluidic networks using electric circuit analogy. Lab Chip *12*, 515–545.

51. Bruus, H. (1997). Theoretical Microfluidics (Oxford University Press). https://doi.org/10.1093/oso/9780199235087.001.0001.

52. Arfaee, M., Kluin, J., and Overvelde, J.T. (2023). Modeling the behavior of elastic pouch motors. In 2023 IEEE International Conference on Soft Robotics (RoboSoft), pp. 1–6. https://doi.org/10.1109/RoboSoft55895.2023.10122046.

53. Zou, S., Picella, S., de Vries, J., Kortman, V.G., Sakes, A., and Overvelde, J.T.B. (2024). A retrofit sensing strategy for soft fluidic robots. Nat. Commun. *15*, 539. https://doi.org/10.1038/s41467-023-44517-z.

54. Liu, T., Chen, Y., Hutchinson, J.W., and Jin, L. (2022). Buckling of viscoelastic spherical shells. J. Mech. Phys. Solids *169*, 105084. https://doi.org/10.1016/j.jmps.2022.105084.

55. Pandey, A., Moulton, D.E., Vella, D., and Holmes, D.P. (2014). Dynamics of snapping beams and jumping poppers. EPL (Europhysics Lett. *105*, 24001. https://doi.org/10.1209/0295-5075/105/24001.

56. Gorissen, B., Melancon, D., Vasios, N., Torbati, M., and Bertoldi, K. (2020). Inflatable soft jumper inspired by shell snapping. Sci. Robot. *5*, eabb1967. https://doi.org/10.1126/scirobotics.abb1967. https://www.science.org/doi/abs/10.1126/scirobotics.abb1967. https://www.science.org/doi/pdf/10.1126/scirobotics.abb1967.

57. Abbasi, A., Yan, D., and Reis, P.M. (2021). Probing the buckling of pressurized spherical shells. J. Mech. Phys. Solid. *155*, 104545. https://doi.org/10.1016/j.jmps.2021.104545. https://www.sciencedirect.com/science/article/pii/S0022509621002039.

58. Lee, A., López Jiménez, F., Marthelot, J., Hutchinson, J.W., and Reis, P.M. (2016). The geometric role of precisely engineered imperfections on the critical buckling load of spherical elastic shells. J. Appl. Mech. *83*, 111005. https://doi.org/10.1115/1.4034431. https://asmedigitalcollection.asme.org/appliedmechanics/article-pdf/83/11/111005/5973058/jam_083_11_111005.pdf.

59. Sobota, P.M., and Seffen, K.A. (2019). Bistable polar-orthotropic shallow shells. R. Soc. Open Sci. *6*, 190888. https://doi.org/10.1098/rsos.190888. https://royalsocietypublishing.org/doi/abs/10.1098/rsos.190888. https://royalsocietypublishing.org/doi/pdf/10.1098/rsos.190888.

60. Morash, V.S., Pensky, A.E.C., and Miele, J.A. (2013). Effects of using multiple hands and fingers on haptic performance. Perception *42*, 759–777. https://doi.org/10.1068/p7443.

61. Cowan, N. (2008). Chapter 20 what are the differences between long-term, short-term, and working memory? In Essence of Memory vol. 169 of *Progress in Brain Research*, W.S. Sossin, J.C. Lacaille, V.F. Castellucci, and S. Belleville, eds. (Elsevier), pp. 323–338. https://doi.org/10.1016/S0079-6123(07)00020-9. https://www.sciencedirect.com/science/article/pii/S0079612307000209.

62. Martin, G., Carlson, N., and Buskist, W. (2010). Psychology (Allyn and Bacon). https://books.google.nl/books?id=4AiArgEACAAJ.

63. Staudacher, E.M., Gebhardt, M., and Dürr, V. (2005). Antennal movements and mechanoreception: Neurobiology of active tactile sensors. Adv. In Insect Phys. *32*, 49–205. https://doi.org/10.1016/S0065-2806(05)32002-9. https://www.sciencedirect.com/science/article/pii/S0065280605320029.

64. Saager, F., and Gewecke, M. (1989). Antennal reflexes in the desert locust schistocerca gregaria. J. Exp. Biol. *147*, 519–532. https://doi.org/10.1242/jeb.147.1.519. https://journals.biologists.com/jeb/article-pdf/147/1/519/2548594/jexbio_147_1_519.pdf.

65. GEWECKE, M. (1970). Antennae: Another wind-sensitive receptor in locusts. Nature *225*, 1263–1264. https://doi.org/10.1038/2251263a0.

66. Lundstrom, M. (2003). Moore's law forever? Science *299*, 210–211. https://doi.org/10.1126/science.1079567. https://www.science.org/doi/abs/10.1126/science.1079567. https://www.science.org/doi/pdf/10.1126/science.1079567.

67. Sitti, M. (2021). Physical intelligence as a new paradigm. Extreme Mech. Lett. *46*, 101340. https://doi.org/10.1016/j.eml.2021.101340. https://www.sciencedirect.com/science/article/pii/S2352431621001012.

68. Sitti, M., Ceylan, H., Hu, W., Giltinan, J., Turan, M., Yim, S., and Diller, E. (2015). Biomedical applications of untethered mobile milli/microrobots. Proc. IEEE *103*, 205–224. https://doi.org/10.1109/JPROC.2014.2385105.

69. Furube, T., Nakashima, D., Matsuda, S., Mikami, K., Hatakeyama, T., Takeuchi, M., Fukuda, K., Ueno, A., Okita, H., Kawakubo, H., et al. (2025). Evaluating stiffness of gastric wall using laser resonance frequency analysis for gastric cancer. Cancer Sci. *116*, 143–151. https://doi.org/10.1111/cas.16383.

70. Kim, K., Edwards, S., Fuxa, K., Lin, H., Shrestha, S., Fan, H., Diaz, N., Berinstein, J., Naik, R., Zhou, Y., and Dong, X. (2025). Mucosa-interfacing capsule for in situ sensing the elasticity of biological tissues. Advanced Materials Technologies *10*, 2401487. https://doi.org/10.1002/admt.202401487. https://onlinelibrary.wiley.com/doi/abs/10.1002/admt.202401487. https://onlinelibrary.wiley.com/doi/pdf/10.1002/admt.202401487.

71. Miskin, M.Z., Cortese, A.J., Dorsey, K., Esposito, E.P., Reynolds, M.F., Liu, Q., Cao, M., Muller, D.A., McEuen, P.L., and Cohen, I. (2020). Electronically integrated, mass-manufactured, microscopic robots. Nature *584*, 557–561. https://doi.org/10.1038/s41586-020-2626-9.

72. Klesh, A.T., Cutler, J.W., and Atkins, E.M. (2012). Cyber-physical challenges for space systems. In 2012 IEEE/ACM Third International Conference on Cyber-Physical Systems, pp. 45–52. https://doi.org/10.1109/ICCPS.2012.13.

73. Dunbabin, M., and Marques, L. (2012). Robots for environmental monitoring: Significant advancements and applications. IEEE Robot. Autom. Mag. *19*, 24–39. https://doi.org/10.1109/MRA.2011.2181683.

74. Luo, D., Maheshwari, A., Danielescu, A., Li, J., Yang, Y., Tao, Y., Sun, L., Patel, D.K., Wang, G., Yang, S., et al. (2023). Autonomous self-burying seed carriers for aerial seeding. Nature *614*, 463–470.

75. Miyaki, Y., and Tsukagoshi, H. (2020). Self-excited vibration valve that induces traveling waves in pneumatic soft mobile robots. IEEE Robot. Autom. Lett. *5*, 4133–4139. https://doi.org/10.1109/LRA.2020.2978455.

76. van Laake, L.C., and Overvelde, J.T.B. (2024). Bio-inspired autonomy in soft robots. Commun. Mater. *5*, 198. https://doi.org/10.1038/s43246-024-00637-7.

77. Patil, V.P., Ho, I., and Prakash, M. (2023). Self-learning mechanical circuits. Preprint at arXiv. https://arxiv.org/abs/2304.08711.

78. Schomaker, H.A.H., Picella, S., Küng Garcia, A., van Laake, L.C., and Overvelde, J.T.B. (2024). Robust phototaxis by harnessing implicit communication in modular soft robotic systems. Adv. Funct. Mater. *34*, 2310932. https://doi.org/10.1002/adfm.202310932. https://advanced.onlinelibrary.wiley.com/doi/abs/10.1002/adfm.202310932. https://advanced.onlinelibrary.wiley.com/doi/pdf/10.1002/adfm.202310932.

79. Robin, A.C. (2004). Paper bag problem. Mathematics today *40*, 104–107.

DEVICE, Volume *3*

Supplemental information

Embodying mechano-fluidic memory in soft machines to program behaviors upon interactions

Alberto Comoretto, Stijn Koppen, Tanaya Mandke, and Johannes T.B. Overvelde

Supplemental Notes

Note S1: Theory of domain analogies and circuit modeling

The goal of modeling the fluidic circuit is to qualitatively capture the experimental results. In particular, the model captures i) effect of component properties on the system-level behavior, e.g. magnitude of after-capacitance affecting frequency and actuator pressure as shown in Fig. 1, ii) long-term memory arising from timed events (such as open/closing of the valves), and iii) transition to short-term memory when the bistable shell is mounted flipped, as shown in Fig. 3.

Utilising the fluidic-electrical analogy [S1], the fluidic system is modeled using both constant and variable linear resistors, linearized capacitors, and hysteretic voltage-controlled switches, allowing to capture complex qualitative behavior using a linear electrical model.

Theory of domain analogies

Engineering systems share the physical phenomenon of the transfer, distribution, and conversion of energy while conserving energy according to the first law of thermodynamics; a common aspect to all systems is the flow of energy and power between components. Multi-domain modeling methods, such as the power bond graph modeling method [S2], exploit this commonality and use the first law and common system features to model multi-domain engineering systems. With some abstraction of governing variables and identification of the common features, one can create useful analogies between different domains, which allows, for example, the analysis of mechanical and/or fluidic systems using electrical circuits.

Irrespective of the domain, components exchange two power conjugate variables called *effort* e and *flow* f. Typically, flow is a so-called through variable, whereas effort is a so-called across variable. Note that the following definitions and derivations follow the standard power bond graph theory [S2]. The product of effort and flow is *power* $\mathcal{P}$ $[\mathrm{W}]$, that is

$$\mathcal{P} = ef. \tag{5}$$

In addition to these power variables, we need two more variables to describe energy storage. These energy variables are generalized *displacement* q, defined as

$$q(t) = \int f \,\mathrm{d}t\,, \quad \text{or} \quad f(t) = \frac{\mathrm{d}q}{\mathrm{d}t}, \tag{6}$$

and generalized *momentum* p defined as

$$p(t) = \int e \,\mathrm{d}t\,, \quad \text{or} \quad e(t) = \frac{\mathrm{d}p}{\mathrm{d}t}. \tag{7}$$

See Table S1 for the definitions of analogous quantities in the mechanical, fluidic, and electrical domains as used throughout this manuscript. Although dedicated bond-graph models do exist for pneumatics (compressible fluids) [S3], these are substantially more complex compared to their incompressible counterparts. As we will elaborate on in more detail in the section 'Modeling fluidic capacitors', the compressibility of air is a dominant contributor to the capacitance of substantial volumes, but its effect on small volume components (such as tubing) is relatively negligible. Hence, we assume incompressibility of the fluid throughout the framework, while taking into account compressibility in key components where it cannot be neglected.

One can model system components using the same elements in all different energy domains. An element is defined by a constitutive law, which is a defining relation between two physical quantities that are two of the four energy and power variables.

In our model, we only use three elements: an effort source, resistors, and capacitors. The inertia element relates flow to momentum and stores kinetic energy. Given the relatively low density of air, the effect of this element is neglected in our model.

A resistor dissipates energy via a loss mechanism, and its constitutive law relates flow to effort, that is $f = f(e)$ or $e = e(f)$ in the general nonlinear case. For a linearized resistor

$$e = Rf, \quad \text{or} \quad f = \frac{1}{R}e, \tag{8}$$

with *resistance* R. The dissipated power is

$$\mathcal{P} = ef = Rf^2 = \frac{e^2}{R}. \tag{9}$$

A capacitor stores potential energy as a function of displacement. The constitutive law of a capacitor relates effort to displacement, that is $e = e(q)$ or $q = q(e)$. For a linear or linearized capacitor

$$q = Ce, \quad \text{or} \quad e = \frac{1}{C}q, \tag{10}$$

with *capacitance* C. In its equivalent integral and derivative forms we have

$$e = \frac{1}{C}\int f \,\mathrm{d}t\,, \quad \text{and} \quad f = C\frac{\mathrm{d}e}{\mathrm{d}t}. \tag{11}$$

The *energy* $\mathcal{E}$ $[\mathrm{J}]$ is the time integral of power, i.e.

$$\mathcal{E}(t) = \int \mathcal{P}\,\mathrm{d}t = \int ef\,\mathrm{d}t\,. \tag{12}$$

The potential energy stored in a capacitor is

$$\mathcal{E}(q) = \int e(q)\frac{\mathrm{d}q}{\mathrm{d}t}\,\mathrm{d}t = \int e(q)\,\mathrm{d}q\,. \tag{13}$$

For a linear capacitor, we have

$$\mathcal{E}(q) = \frac{1}{C}\int q\,\mathrm{d}q = \frac{q^2}{2C} = \frac{1}{2}Ce^2. \tag{14}$$

Modeling fluidic resistors

Following the definition of a resistor in the previous section, a fluidic resistor relates the *pressure* drop p (fluidic effort) across a component to the *volumetric flow rate* Q (fluidic flow) through it, that is $p = p(Q)$ in general. The following derivations are textbook material [S4], and are reported here for clarity.

For example, the fluidic resistance of a long cylindrical pipe of constant cross section constituting an incompressible and Newtonian fluid in laminar flow is given by the Hagen-Poiseuille equation:

$$p = RQ, \tag{15}$$

with *fluidic resistance* being

$$R = 8\pi\frac{\mu L}{A^2}, \tag{16}$$

where L the length of the pipe, μ the dynamic viscosity of the medium, and A the cross-sectional area of the pipe. Such linearized fluidic resistance dissipates power as

$$\mathcal{P} = pQ = RQ^2. \tag{17}$$

The use of this linear relationship is, in principle, limited to incompressible, laminar, and steady flow, none of which are effectively satisfied in the relevant experimental conditions in this work. In addition, pressure drops resulting from changes and components in a piping system (e.g., sudden enlargement or contractions, bends, entrance effects, and pipe fittings), so-called minor losses, are typically roughly proportional to the square of the flow rate [S5]. In addition, for compressible media as used in pneumatics, the volumetric flow rate is dependent on the change in density due to compressibility.

To approximately capture the qualitative behavior of the system with a simple model, we neglect these effects, and we linearize the nonlinear behaviors of the individual components around the expected working regime. For example, we consider a resistor that we expect to operate between pressures p_1 and p_2. We characterize the resistor and read the corresponding flows Q_1 and Q_2, and define the linearized resistance of the component by

$$R = \frac{\Delta p}{\Delta Q} = \frac{p_2 - p_1}{Q_2 - Q_1}. \tag{18}$$

We now clarify our usage of the physical units throughout. The pressure measured in the experimental characterization and the values provided in Table S2 and Table S3 are in units of kPa. The volumetric flow rate in the experimental characterizations is measured in so-called *standard liters per minute* (SLPM). The SLPM is a unit of flow rate of a gas at standard conditions for temperature and pressure. Since 1982, standard temperature and pressure is defined as a temperature of $T_0 = 273.15\,\mathrm{K}$ ($0\,^\circ\mathrm{C}$) and an absolute pressure of $p_0 = 100\,\mathrm{kPa}$ ($1\,\mathrm{bar}$) [S6]. Conversion from SLPM to $\mathrm{L\,min^{-1}}$ is via

$$1\ \text{SLPM} = \frac{T_0}{T}\frac{p}{p_0}\mathrm{L\,min^{-1}}. \tag{19}$$

Throughout the article, we assume isothermal conditions, that is, $T \approx T_0$. To retain the linearity of the model, we neglect the effect of pressure difference on the measured flow rate, that is, we assume $p \approx p_0$, and thus 1 SLPM $\approx 1\ \mathrm{L\,min^{-1}}$. Consequently, the measured resistances in Table S2 and Table S3 are provided in units of $\mathrm{kPa/L/min}$. Thus, in contrast to using standard metric units, for closer alignment between model and experiments and to retain values of practical relevance and understanding, we choose to work with units of kPa and $\mathrm{L\,min^{-1}}$ throughout the manuscript, both in experiments and in models.

We can now model the linearized fluidic resistors in an analogous electrical circuit using the fluidic-electrical analogy of a resistor [S1]. In the electrical domain, a resistor is governed by Ohm's law, which states that the *voltage* across a conductor V is directly proportional to the *current* I flowing through it via *electrical resistance* R $[\Omega]$, i.e.

$$V = RI. \tag{20}$$

Modeling fluidic capacitors

Following the definition of a capacitor in the first section, a fluidic capacitor is an element that relates pressure p to volume V, that is $p = p(V)$ or $V = V(p)$. For a linear or linearized capacitor, the change in volume is proportional to pressure drop, that is

$$V = Cp, \tag{21}$$

with *total fluidic capacitance* C [S4]. Taking the time derivative on both sides, this can be rewritten in terms of power variables, that is, a proportional relationship between the volumetric flow rate Q and the rate of pressure change $\frac{\mathrm{d}p}{\mathrm{d}t}$, namely

$$Q = C\frac{\mathrm{d}p}{\mathrm{d}t}, \quad \text{or} \quad p = \frac{1}{C}\int Q\,\mathrm{d}t\,. \tag{22}$$

Such linearized capacitor stores potential energy as:

$$\mathcal{E}(V) = \frac{V^2}{2C}. \tag{23}$$

In what follows, we further analyze the meaning of *total fluidic capacitance* [S7]. Consider thereto a deformable component of volume V filled with a gas of density ρ, which both depend on the internal pressure but not on temperature (as we assume isothermal conditions). By conservation of mass, the mass flow rate in or out of the component is

$$\begin{aligned}\frac{\mathrm{d}m}{\mathrm{d}t} &= \frac{\mathrm{d}\rho}{\mathrm{d}t}V + \rho\frac{\mathrm{d}V}{\mathrm{d}t} \\ &= \frac{\partial\rho}{\partial p}\frac{\mathrm{d}p}{\mathrm{d}t}V + \rho\frac{\partial V}{\partial p}\frac{\mathrm{d}p}{\mathrm{d}t} \\ &= \left(\frac{\partial\rho}{\partial p}V + \rho\frac{\partial V}{\partial p}\right)\frac{\mathrm{d}p}{\mathrm{d}t}.\end{aligned} \tag{24}$$

The bulk modulus of the gas K, i.e., a measure of the resistance of substance to bulk compression, is defined as the ratio of the pressure increase to the resulting relative decrease in volume, that is

$$K = -V\frac{\partial p}{\partial V} = \rho\frac{\partial p}{\partial \rho}, \tag{25}$$

since volume is inversely proportional to the density. Consequently, one can deduce that

$$\frac{\partial\rho}{\partial p} = \frac{\rho}{K}. \tag{26}$$

Substitution of Eq. (26) in Eq. (24) yields

$$\begin{aligned}\frac{\mathrm{d}m}{\mathrm{d}t} &= \rho\left(\frac{V}{K} + \rho\frac{\partial V}{\partial p}\right)\frac{\mathrm{d}p}{\mathrm{d}t} \\ &= \rho Q\end{aligned} \tag{27}$$

with, as per the definition of capacitance in Eq. (22) ($Q = C\frac{\mathrm{d}p}{\mathrm{d}t}$), we identify

$$C = \frac{V}{K} + \frac{\partial V}{\partial p} \tag{28}$$

as the total fluidic capacitance with summed contributions from (i) the compressibility of the gas and (ii) the change in volume of the container as a consequence of elasticity [S4]. Assuming an ideal gas, the equation of state is

$$p = \rho R T, \tag{29}$$

with specific gas constant R. It follows that the bulk modulus under isothermal conditions is

$$K = \rho\frac{\partial p}{\partial \rho} = \rho R T = p, \tag{30}$$

that is, the bulk modulus of an ideal gas is equal to its pressure.

All capacitor components consist of, at least to some extent, both contributions of capacitance, and these typically depend nonlinearly on the pressure. Especially when working with a compressible medium such as air, even the various connecting tubes have non-negligible capacitance. Similarly to the resistors, for simplicity, we only consider the dominant contributions (that are the large chambers) and linearize them around the working conditions. To retain linearity, we also approximate the bulk modulus as constant and equal to atmospheric pressure, so $K \approx p_0$.

Specifically, the inextensible pouches have a highly nonlinear volume-pressure relationship (Fig. S6), which consists of mainly two regimes: an approximately zero stiffness regime at low pressure and a stiff regime when inflated. Within the working conditions, the pouches are used solely in the inflated regime. In this regime, the change in volume as a consequence of pressure is relatively small, and hence, we can neglect this contribution to the capacitance. That is, we model the pouches as rigid tanks with geometric volume V_{pouch} and bulk modulus K. Consequently, we model the pouches as linear fluidic capacitors with capacitance

$$C_{\text{pouch}} \approx \frac{V_{\text{pouch}}}{p_0}. \tag{31}$$

See Table S2 for the values used for pre- and after-capacitance C_{p} and C_{a}, respectively.

The actuator is itself a capacitor with an initial volume V_{act}. However, its volume changes considerably due to the deformation of the material when pressurized. Consequently, both contributions of change of density and change of volume should be considered. Upon linearization of the latter effect, the actuator can be modeled as a linear fluidic capacitor with capacitance

$$C_{\text{act}} \approx \frac{V_{\text{act}}}{p_0} + \frac{\Delta V}{\Delta p}, \tag{32}$$

with ΔV and Δp the changes in volume and pressure in the working regime. In our model, we use the value of the capacitance of the actuator C_{act} as a fitting parameter to confer the contributions of change of density, change of volume, as well as remaining parasitic capacitances (e.g., compressibility of air within the connecting tubes). In Table S2, we report the fitted values as underlined numbers.

Recall the definition of capacitance relating flow rate and rate of change of pressure in Eq. (22), i.e. $Q = C\frac{\mathrm{d}p}{\mathrm{d}t}$, where Q has units of $\mathrm{L\,min^{-1}}$ and $\frac{\mathrm{d}p}{\mathrm{d}t}$ units of $\mathrm{kPa\,s^{-1}}$. Note that for convenience, we provide capacitances in units of $\mathrm{mL/kPa}$. For consistency, the capacitance values must be converted from $\mathrm{mL/s/kPa/s}$ to $\mathrm{L/min/kPa/s}$ by multiplication of the provided capacitance values by a conversion factor

$$\alpha = \frac{60\,\mathrm{s}}{1000\,\mathrm{mL}}. \tag{33}$$

Without further notice, all presented capacitance values are multiplied by this conversion factor when implemented in the LTspice® simulations.

We can now model the linearized fluidic capacitors in an equivalent electrical circuit using the fluidic-electrical analogy of a capacitor [S1]. In the electrical domain, a capacitor relates the charge q [C] of the capacitor directly proportional to the voltage V across the capacitor via *electrical capacitance* C [F] (or, equivalently the current $I = \frac{\mathrm{d}q}{\mathrm{d}t}$ [A] through the capacitor to the time rate of change of voltage V over the capacitor), i.e.

$$q = CV, \quad \text{or} \quad I = C\frac{\mathrm{d}V}{\mathrm{d}t}. \tag{34}$$

Modeling the hysteretic valve and the bistable capacitor

To model the hysteretic nature of pressure-dependent snapping of mechanical components, as found in the hysteretic valve and the bistable shell, we use voltage-controlled switches. By doing so, we assume the events are instantaneous, and intermediate states are not represented. By introducing hysteresis directly in the opening and closing threshold of the switches, we capture the hysteresis in the snap-forward and snap-back of the nonlinear components.

Following our previous work [S8], we model the soft hysteretic valve as a normally-closed voltage-controlled hysteretic switch with trip opening and closing pressures $p_{\text{hv,o}}$ and $p_{\text{hv,c}}$ (Fig. S2). These opening and closing pressures values are obtained from experimental characterization under quasi-static conditions that we performed in previous work [S9]. The hysteretic voltage-controlled switch compares the opening and closing pressure to the control pressure. The control pressure is the pressure difference between the two sides of the valve, that is, the difference between the upstream pressure and the (downstream) actuator pressure, that is $p_{\text{hv,c}} = p_{\text{pre}} - p_{\text{act}}$. The resistance of the hysteretic valve in open condition R_{hv} is obtained via linearization of the experimentally characterized curve in our previous work [S9].

We model the mechano-fluidic bistable capacitor as a rigid tank with volume V_{bs} and corresponding constant capacitance C_{bs}. This constant capacitance is accessible to either of the pressure lines (the after pressure p_{after} or the venting pressure p_{vent}) via two coupled hysteretic voltage-controlled switches (Fig. S8). One of the switches is normally open, whereas the other switch is normally closed. These switches are coupled by sharing the same control pressure $p_{\text{bs,c}}$. For the long-term memory circuit, the control pressure is

$$p_{\text{bs,c}} = p_{\text{after}} - p_{\text{vent}}. \tag{35}$$

Instead, for the short-term memory circuit, the control pressure is redefined as

$$p_{\text{bs,c}} = p_{\text{vent}} - p_{\text{after}}. \tag{36}$$

The switches trip at opening and closing pressure $p_{\text{bs,o}}$ and $p_{\text{bs,c}}$, respectively, in accordance with the experimentally obtained snapping values under quasi-static conditions (Fig. S6). Importantly, note that we model the short-term memory circuit by i) swapping the normally open and normally closed switches and by ii) redefining the control pressure according to Eq. (36), to represent the physical flipping of the bistable shell (Fig. 3).

As a consequence, at any instant, the large geometric capacitor is accessible from one of the two sides, effectively simulating instantaneous (dis)appearance of the capacitance at the switching pressures that correspond to the snapping pressures. Note that intermediate states cannot be represented, which would require a more detailed model of the elastic shell, including the intermediate negative stiffness curve (white dots in Fig S6). In addition, depending on the specific time of switching, the capacitor may be (partially) charged, and, nonphysically, this energy would be available to the other pressure line. The influence of this effect (about one to two consecutive oscillations), however, occurs at a time-scale much smaller than the time-scale of interest (tens to hundreds of oscillations).

LTspice® simulations

With the assumptions and definitions from the previous sections, we can model the fluidic circuits as electronic circuits using the LTspice® software (Analog Devices Inc.).

In Figure S2, we report the LTspice® circuit that models the fluidic circuit in Figure 1. The parameters used in the model are summarized in Table S2, where the non-underlined values are obtained directly from the experimental characterization of the individual components, while the

underlined values are obtained from visually fitting the simulation results to the experimental results. As a fitting criterion, we visually align the curves i) frequency function of after capacitance, ii) maximum actuator pressure function of after capacitance, and iii) minimum actuator pressure function of after capacitance (Fig. S3). In particular, the pre-resistance R_{p} is fitted such that the oscillation frequencies match, and the after resistance R_{after} is fitted such that the minimum and maximum actuator pressures p_{after} match. Importantly, we observe that the model captures the experimental trends of i) decrease in frequency for larger after-capacitance volume (Fig. S3A), ii) decrease of maximum actuator pressure and increase of minimum actuator pressure for larger after-capacitance volume (Fig. S3B), and iii) an overall decrease in pressure difference at the actuator (that corresponds to a decrease in actuator stroke) for larger after-capacitance volume (Fig. S3C).

In Figure S8, we depict the LTspice® circuit that simulates the long- and short-term memory circuits in Figure 3. In addition to the elements already present in the simpler model (Fig. S2), we introduce i) the bistable shell modeled as two hysteretic switches that access a fixed capacitance (see previous section) and ii) normally open and normally closed valves. We model interactions with the valves as time-dependent variable linear resistors with resistance $R = R(t)$, where $R(t)$ is a pulse wave that takes a high value ($10\,\mathrm{GPa/L/min}$) to represent a closed valve, and a low value ($10\,\mathrm{Pa/L/min}$) to represent an open channel. The parameters used in the model of Figure S8 are reported in Table S3, together with the parameters inherited from the simpler model in Table S2.

In Figure S8, we report the results of the simulations compared to the results from the experiments. First, we note how the model captures the long-term memory effect when alternatively opening and closing the valves (Fig. S9A,B). Second, we observe that the model captures the transition to the short-term memory behavior when the shell is physically flipped in its holder (modeled as a swapping of the hysteretic switches) (Fig. S9C,D). Third, we observe that the short-term memory model captures the experimental trend of increase in memory-retention time for increased venting resistance (Fig. S9E,F). Lastly, a limitation of the model is that the intermediate phase between the initiation and the ending of the snap-back (Fig. S9D between $\sim 0.9\,\mathrm{min}$ and $\sim 1.5\,\mathrm{min}$) is not captured. Rather, the modeled circuit directly snaps back (Fig. S9C at $\sim 1\,\mathrm{min}$). This is a result of modeling the bistable shell with ideal hysteretic switches, which do not display the negative-stiffness regime typical of the real shells (white dots in Figure 2E).

Supplemental Tables

Table S1: **Analogous quantitity definitions in multi-domain analysis.**

Domain	Effort e	Flow f	Displacement q
Mechanical	Force F [N]	Velocity v [$\mathrm{m\,s^{-1}}$]	Distance x [m]
Fluidic	Pressure P [Pa]	Flow rate Q [$\mathrm{m^3\,s^{-1}}$]	Volume V [$\mathrm{m^3}$]
Electrical	Voltage V [V]	Current I [A]	Charge q [C]

Table S2: **Parameters used in the LTspice® model in Figure S2 of the fluidic circuit in Figure 1.** The columns correspond to parameters definitions, symbols, values, and units. Non-underlined values are directly obtained from experimental characterization, while underlined values are obtained from visual fitting of the model to the curves, as per Figure S3.

Parameter	Symbol	Value	Unit
Source pressure	p_{source}	130	kPa
Pre-resistance	R_{pre}	$\underline{35}$	kPa/L/min
Pre-capacitance	C_{pre}	0.6	mL/kPa
Hysteretic valve opening pressure	$p_{\text{hv,o}}$	70	kPa
Hysteretic valve closing pressure	$p_{\text{hv,c}}$	3	kPa
Hysteretic valve open resistance	R_{hv}	0.5	kPa/L/min
After-capacitance	C_{after}	$0-0.4$	mL/kPa
Actuator capacitance	C_{act}	$\underline{0.6}$	mL/kPa
After-resistance	R_{after}	$\underline{6}$	kPa/L/min

Table S3: **Parameters used in the LTspice® model in Figure S8 of the fluidic circuits in Figure 3.** The columns correspond to parameters definitions, symbols, values, and units. These values are obtained directly from the experimental characterization of the individual components. Note that, in addition to the parameters in this table, the model of the circuits in Figure S8 also inherits the parameters (Table S2) of the simpler model of Figure S2.

Parameter	Symbol	Value	Unit
Bistable shell capacitance	C_{bs}	0.34	mL/kPa
Bistable shell opening pressure	$p_{\text{bs,o}}$	35	kPa
Bistable shell closing pressure	$p_{\text{bs,c}}$	-5	kPa
Venting resistance in long-term memory	$R_{\text{v,ltm}}$	125	kPa/L/min
Venting resistance in short-term memory	$R_{\text{v,stm}}$	$322-4542$	kPa/L/min

Supplemental Figures

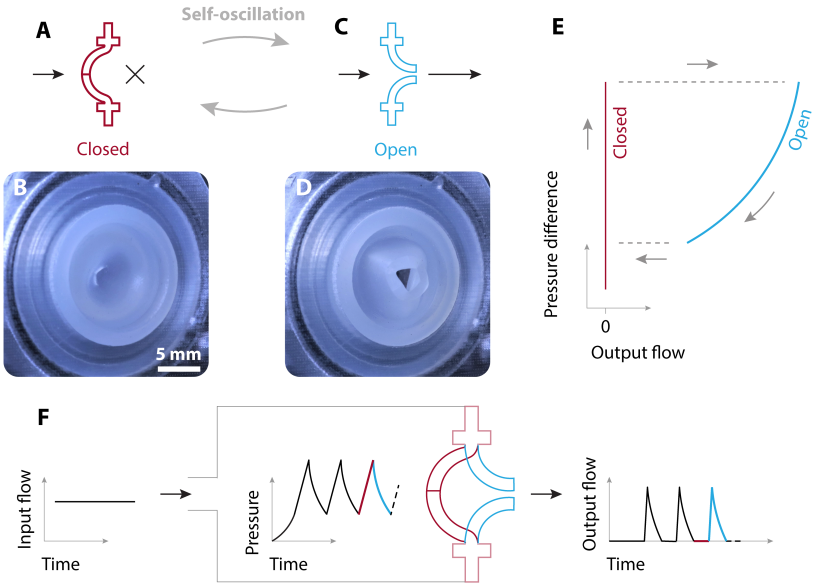

Figure S1: **The hysteretic valve self-oscillates given constant input flow.** The hysteretic valve is an elastic shell with a slit at the apex. (**A**) Valve in closed state: when pressure builds up, the slit is closed, and output flow is not provided. (**B**) Photograph of the closed valve as seen from the outlet side. (**C**) Valve in open state: when the shell snaps to the collapsed state, the slit opens, allowing flow in output. (**D**) Photograph of the open valve. (**E**) Relationship between the output flow and the pressure difference across the valve. When the shell is in the rest state (valve closed), pressure builds up with zero flow in output. When the pressure reaches the snap-through value, the shell snaps (valve opens). When the valve is in the open state, it acts as a nonlinear fluidic resistance that vents flow in output, hence, pressure decreases. When pressure decreases past the snap-back value, the shell snaps back to the rest state (valve closes). (**F**) When placed in a fluidic circuit with constant flow in input, the valve behaves as a relaxation oscillator [S7], continuously transitioning between the closed state and the open state. The upstream pressure oscillates between a low and a high value, and the output flow alternates between zero and positive bursts. Adapted with permission under CC BY from Van Laake and Comoretto et al. [S8].

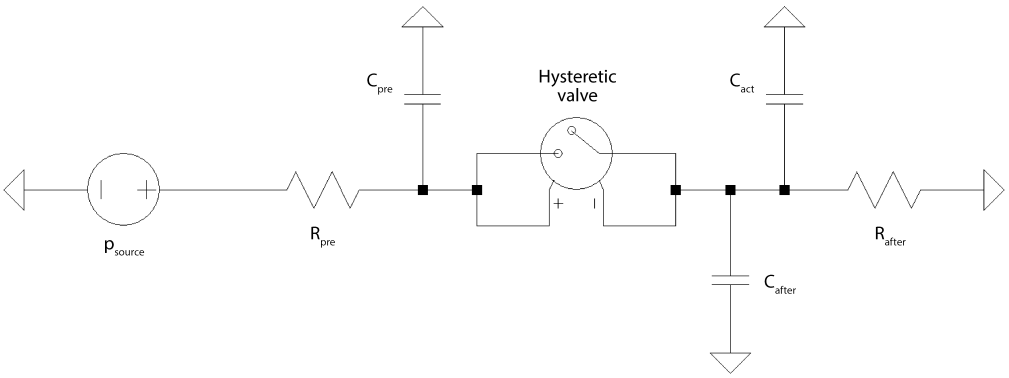

Figure S2: **LTspice® model of the fluidic circuit in Figure 1.** Using the fluidic-electrical analogy (Note S1), we model the fluidic circuit of the relaxation oscillator as an electronic circuit. The pressure source is a voltage source, the hysteretic valve is a voltage-controlled hysteretic switch, fluidic constrictions are resistors, and fluidic chambers are capacitors. The parameters used in this model are reported in Table S2.

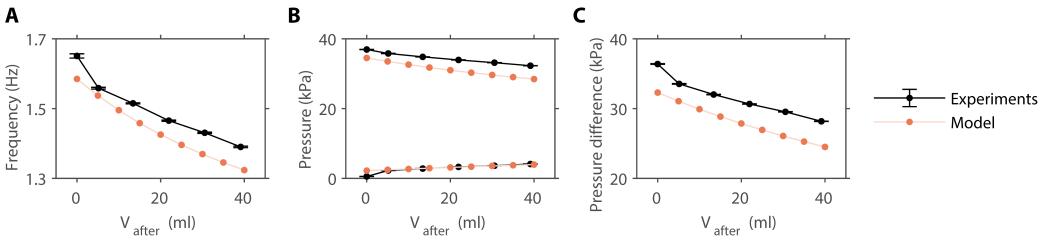

Figure S3: **The model captures the experimental trends of the fluidic relaxation oscillator in Figure 1.** (**A**) Oscillation frequency decreases for a larger volume of the after-capacitance. (**B**) Maximum actuator pressure decreases, and minimum actuator pressure increases for a larger volume of the after-capacitance. The top data points correspond to the maximum pressure during the oscillation, and the bottom to the minimum pressure. (**C**) Pressure difference in the actuator decreases for a larger volume of the after-capacitance.

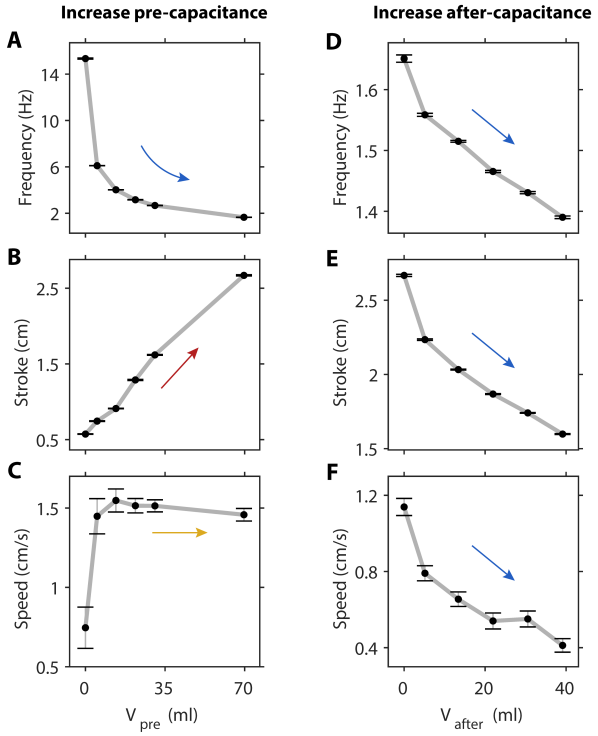

Figure S4: **Response of the crawler in Figure 1 as a function of pre- and after-capacitances.** We vary the pre- and after-capacitances of the circuit in the single-actuator machine (Fig. 1) by manufacturing various inextensible pouches (Methods) with different height and width (Fig. S13). In particular, all the pouches have a fixed width of $30\,\mathrm{mm}$, and we vary their height from $30\,\mathrm{mm}$ to $150\,\mathrm{mm}$ in increments of $30\,\mathrm{mm}$. In the case of the pre-capacitance, we also test a larger value of volume ($70\,\mathrm{mL}$), as the sum of a pouch with height $120\,\mathrm{mm}$ and one with height $150\,\mathrm{mm}$. The values of geometric volume reported in this figure result from applying Eq. (2). The frequency and vertical stroke of the actuator are measured in a benchtop experiment, with the actuator not interacting with the surroundings. The speed of the machine is measured by recording the crawler from above, and detecting the ArUco marker (Methods). (**A**) Frequency of activation of the actuator, (**B**) vertical stroke of the actuator, and (**C**) speed of the machine as a function of pre-capacitance. (**D**) Frequency of activation of the actuator, (**E**) vertical stroke of the actuator, and (**F**) speed of the machine as a function of after-capacitance. Increasing the pre-capacitance volume causes a decrease in frequency (blue arrow in A) and an increase in stroke (red arrow in B), resulting in a negligible change in speed (yellow arrow in C) for positive pre-capacitance volumes. In contrast, increasing the after-capacitance causes a decrease in both the frequency and stroke of the actuator, leading to a net decrease in the resulting speed of the machine (blue arrows in D, E, F).

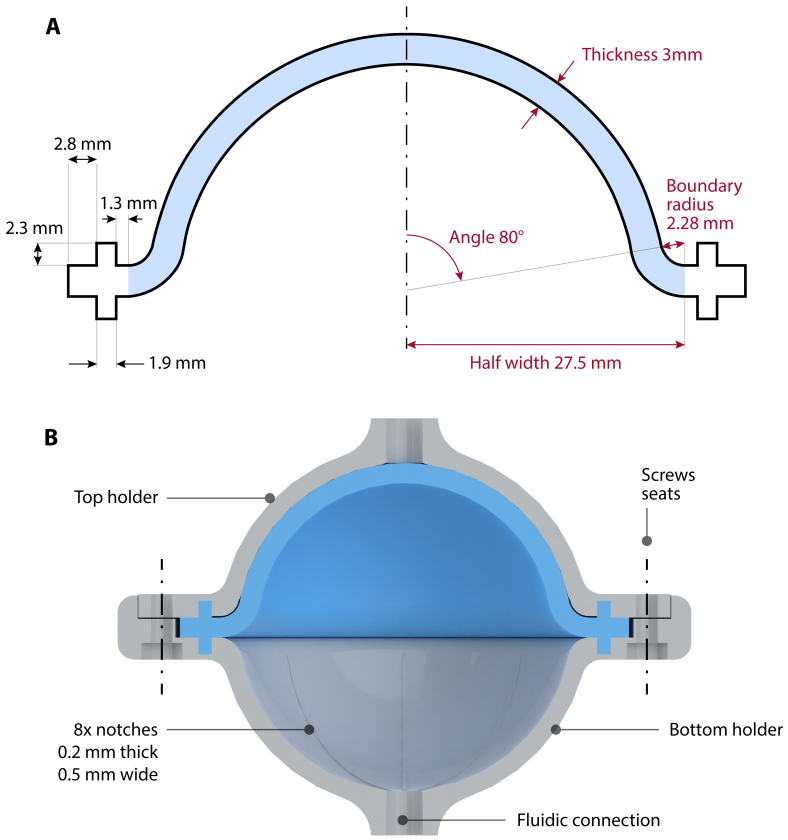

Figure S5: **Design of the bistable elastic shells.** (**A**) Schematic of the cross-section of the shell, with the unclamped section highlighted in blue, and the clamped section highlighted in white. The design parameters that affect the behavior of the shell when pressurized are the thickness, the shallowness angle, the width, and the boundary radius (red annotations). The shells used throughout the article have thickness $3\,\mathrm{mm}$, angle $80°$, width $55\,\mathrm{mm}$, and boundary radius $2.28\,\mathrm{mm}$. Practically, to clamp the shell in a rigid holder, we designed an extension on the outer edge consisting of a rim and a notch (black annotations). (**B**) Render of a cross-section view of the shell in its holder. The holder presents 8 notches on the inside of each rigid shell, to ensure that the air provided through the fluidic connections distributes pressure evenly on the surface of the silicone shell. The holder has 6 holes, placed radially outside the shell, used to clamp the shell in place using M3 screws and nuts.

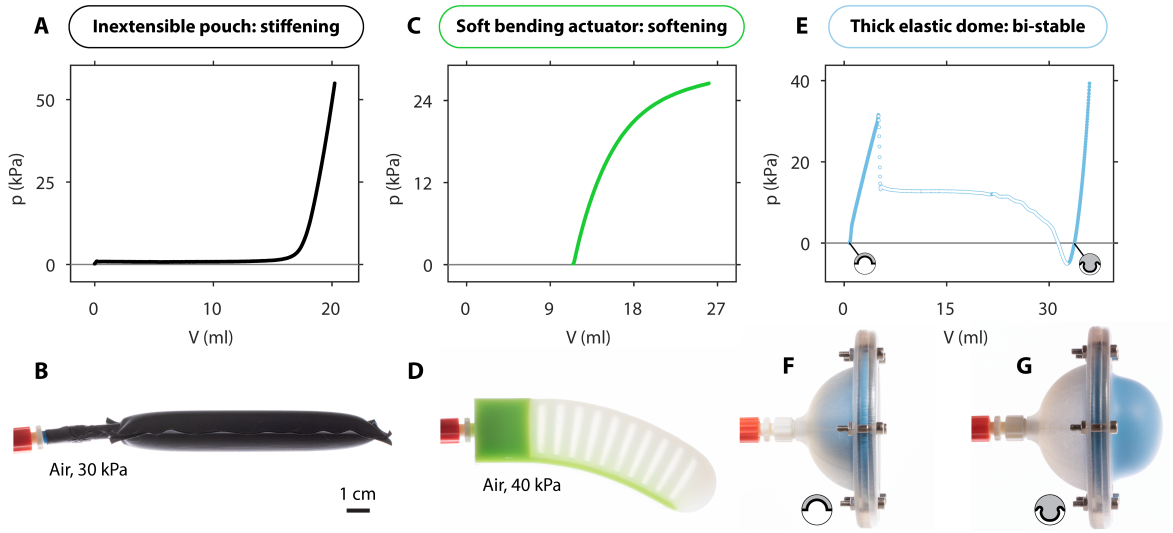

Figure S6: **Pressure-volume curves of a pouch, an actuator, and a bistable shell.** We inflate three distinct fluidic capacitors under quasi-static volume-control conditions. We do so by slowly injecting a controlled volume of water that corresponds to the geometric volume inside the capacitors, since water is incompressible; while increasing volume, we measure pressure (Methods). (**A**) The pressure-volume curve of an inextensible pouch with width $30\,\mathrm{mm}$ and height $120\,\mathrm{mm}$. Note that pressure starts to substantially increase only when the volume reaches $\sim 15\,\mathrm{mL}$. (**B**) Photograph of the pouch pressurized with air at $30\,\mathrm{kPa}$. (**C**) The pressure-volume curve of a soft bending actuator. There is an initial volume at atmospheric pressure corresponding to the geometric volume of the inner chambers. (**D**) Photograph of the soft bending actuator pressurized with air at $40\,\mathrm{kPa}$. (**E**) The pressure-volume curve of our bistable elastic shell. White markers indicate the negative stiffness branch (where an increase in volume causes a decrease in pressure). For increasing volume, pressure is non-monotonous: pressure first increases then decreases, then increases again. Note that the positive-stiffness branches intersect the zero-pressure vertical line at two points: the system is bistable, as it is stable in both these two states without applying pressure. (**F**) Photograph of the bistable shell in the rest state (volume $0.8\,\mathrm{mL}$, zero pressure). (**G**) Photograph of the bistable shell in the snapped state (volume $34\,\mathrm{mL}$, zero pressure).

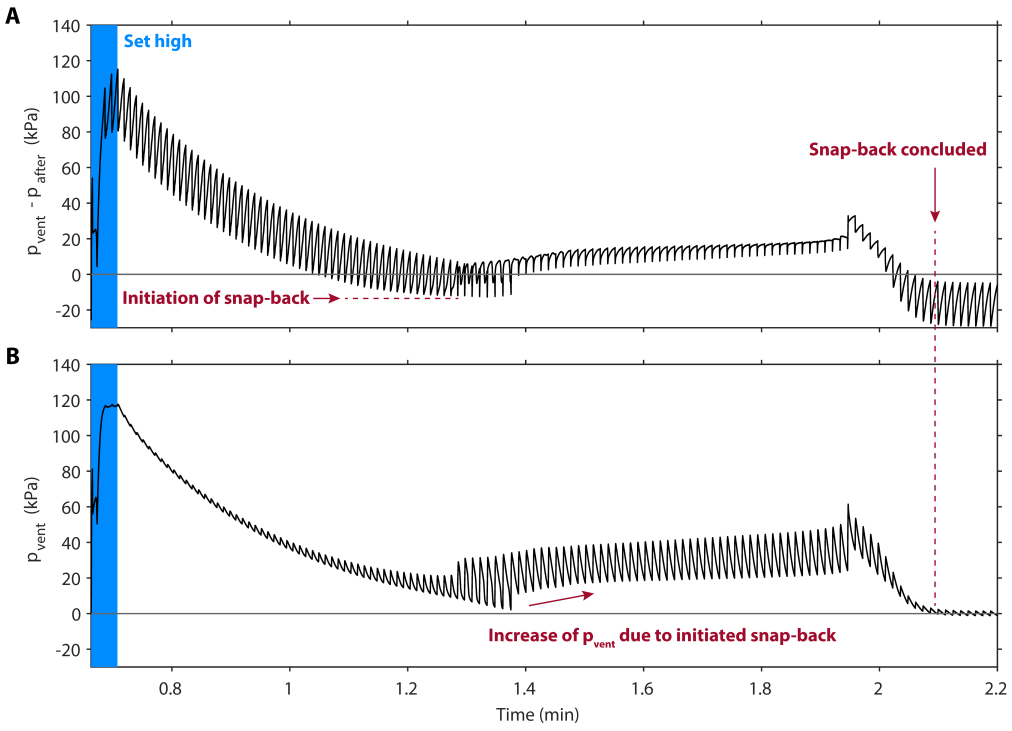

Figure S7: **In the short-term memory circuit in Figure 3, the spontaneous snap-back is not instantaneous.** (**A**) The pressure difference between the venting chamber and the chamber after the hysteretic valve ($p_{\mathrm{vent}} - p_{\mathrm{after}}$) decreases in time after the system is set to the snapped state, because air in the venting chamber vents to atmosphere through the venting resistance R_{vent}. Since the hysteretic valve oscillates, this pressure difference oscillates as well, while decreasing. When the pressure difference reaches the snap-back pressure of the shell, the shell initiates the snap-back. (**B**) After the shell initiates the snap-back, pressure in the venting chamber p_{vent} increases, because of the relatively high venting resistance R_{vent} connected to the venting chamber. This happens because the shell deforms towards the venting chamber, effectively compressing the air that does not immediately vent through the high resistance. Approximately $50\,\mathrm{s}$ after the initiation of the snap-back, the shell completes the snap-back (p_{vent} drops to zero).

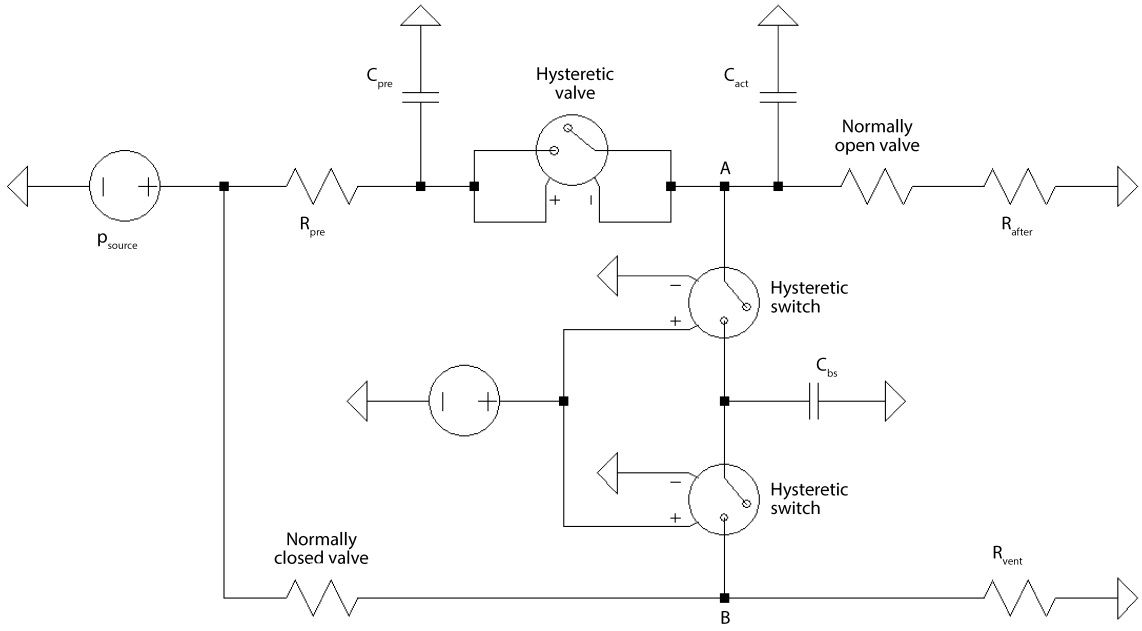

Figure S8: **LTspice® model of the fluidic circuits in Figure 3.** Using the fluidic-electrical analogy (Note S1), we model the fluidic circuits that give rise to the long- and short-term memory. Compared to the model in Fig. S2, we add the bistable capacitor. We model this bistable element as an after-capacitance, of which the access is controlled by voltage-controlled hysteretic switches. This control voltage is the voltage drop across the two switches (between node A and node B). The parameters used in this model are reported in Table S3.

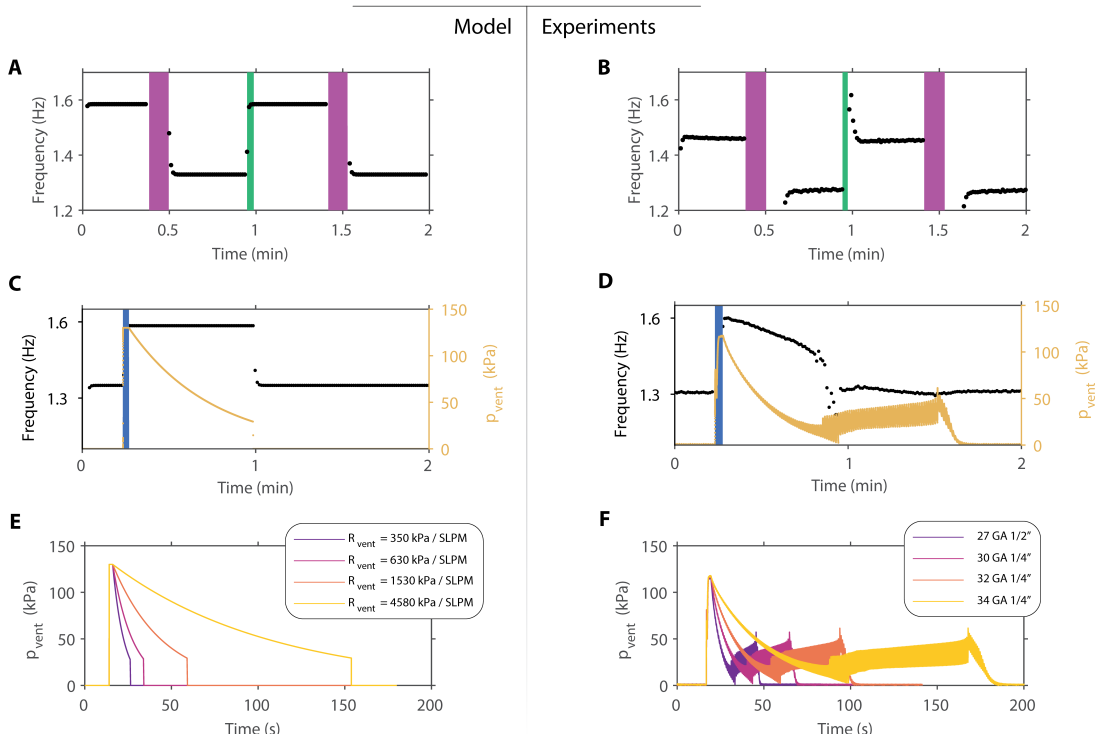

Figure S9: **The model captures the long-term and short-term memory of Figure 3.** Evolution of the oscillation frequency in the long-term memory circuit when alternatively closing the NO valve (purple) and opening the NC valve (green) (**A**) in the model and (**B**) in the experiment. Evolution of the oscillation frequency and of the venting pressure in the short-term memory circuit after opening the NC valve (blue) (**C**) in the model and (**D**) in the experiment. Evolution of the venting pressure in the short-term memory circuit, for increasing venting resistances, (**E**) in the model and (**F**) in the experiment.

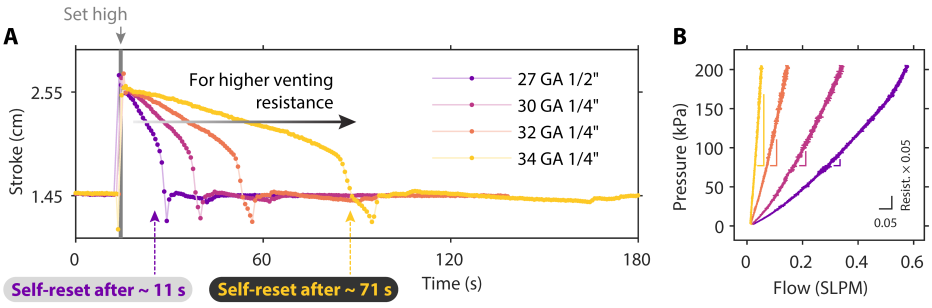

Figure S10: **In the short-term memory circuit in Figure 3, increasing the venting resistance leads to a higher memory-retention time.** We test the short-term memory circuit (Fig. 3) for different values of venting resistance (different commercial needles, Metcal). In a benchtop setup (Methods) we measure the vertical stroke of the actuator in time. (**A**) After opening the normally closed valve, the memory element snaps, and the system is set to the high-stroke state. In the case of the lowest resistance tested (27 Gauge, 0.5 in needle), the system self-resets to the low state (the shell snaps back) after $\sim 11\,\mathrm{s}$ (purple line). For higher venting resistance, the time required to self-reset (memory-retention time) increases. In the case of the highest resistance tested (34 Gauge, 0.25 in needle), the memory-retention time is $\sim 71\,\mathrm{s}$ (yellow line). (**B**) The pressure-flow curves of the tested resistances show that, as expected, the resistance increases with increasing Gauge number of the needles.

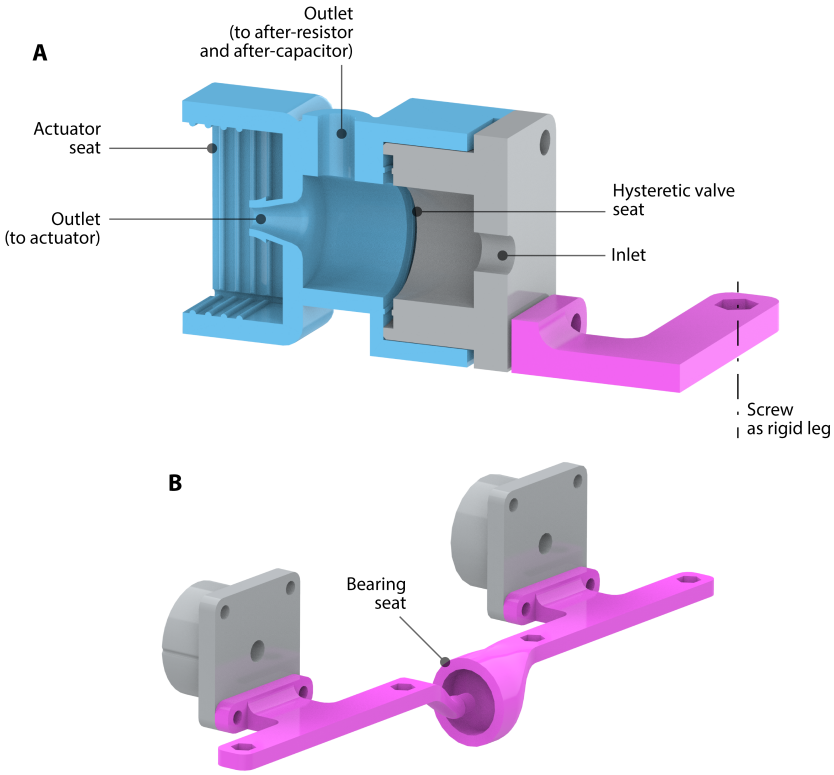

Figure S11: **Design of the machines.** (**A**) Cross-section view of the main module to which the rest of the components are connected to assemble the single-actuator machine. The hysteretic valve is seated between the inlet part (grey) and the outlet part (blue). The bending actuator connects to the outlet part via press-fit. An additional part (pink) connects to the inlet part, to allow for screws to be placed as rigid legs. (**B**) The two-actuator machine presents two mirrored copies of the single-actuator assembly, with the only difference being the rigid-legs parts (pink). These parts accommodate a bearing, to allow relative rotation of the two parts with respect to each other.

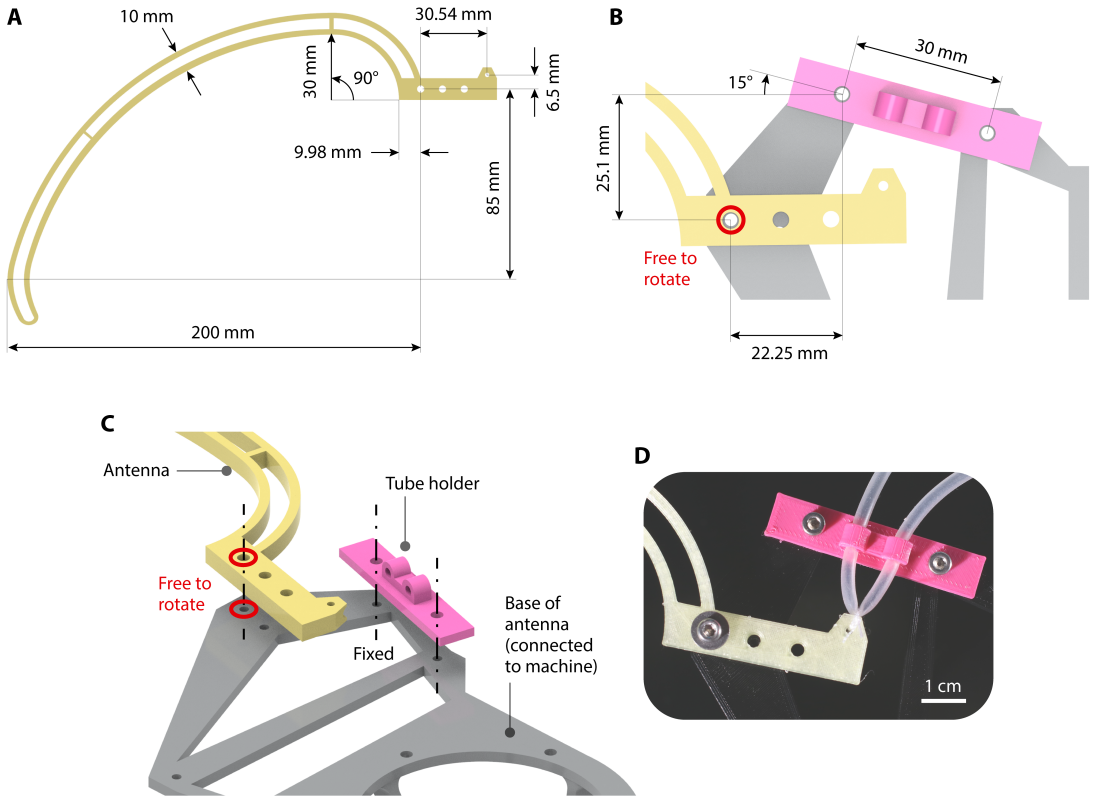

Figure S12: **Design of the antenna.** (**A**) Relevant design parameters of the rigid antenna in Figure 6. (**B**) Design parameters of the hinge, with the antenna (yellow) connected to the base (grey) through a loose screw that allows rotation (red mark). (**C**) Indication of the mounting holes of the antenna (yellow) and the tube holder (pink) to the base (grey). (**D**) Photograph of the assembled hinge, with the antenna (yellow) firmly attached to the silicone tube (inner diameter $2.5\,\mathrm{mm}$, thickness $0.4\,\mathrm{mm}$, length $30\,\mathrm{mm}$, and inlet-outlet distance $10\,\mathrm{mm}$) with a thin thread.

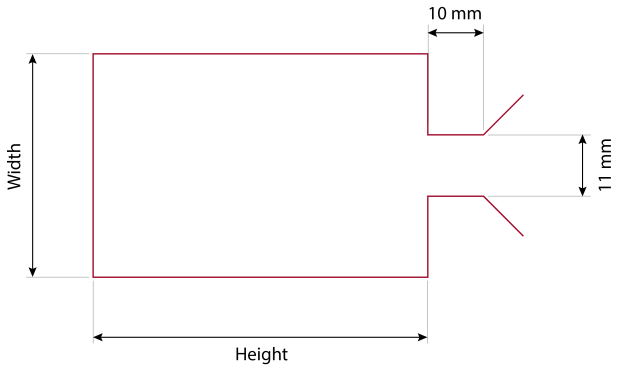

Figure S13: **Design of the inextensible pouches.** The pouches are rectangular, with an opening at one of the shorter sides. An Adobe Illustrator file, containing the red lines reported here, is used to generate the G-code. The 3D printer follows this path to seal two TPU sheets together (Methods).

Supplemental References

[S1] Oh, K.W., Lee, K., Ahn, B., and Furlani, E.P. (2012). Design of pressure-driven microfluidic networks using electric circuit analogy. Lab on a Chip *12*, 515–545.

[S2] Borutzky, W. (2009). Bond graph methodology: development and analysis of multidisciplinary dynamic system models. Springer Science & Business Media.

[S3] Sakurai, Y., and Takahashi, K. (2004). Proposal of a new bond-graph method for modelling pneumatic systems. International Journal of Fluid Power *5*, 17–23.

[S4] Bruus, H. (1997). Theoretical Microfluidics. Oxford University Press. ISBN 978-0-19-923508-7. https://doi.org/10.1093/oso/9780199235087.001.0001. 10.1093/oso/9780199235087.001.0001.

[S5] Welty, J., Rorrer, G.L., and Foster, D.G. (2014). Fundamentals of momentum, heat, and mass transfer. John Wiley & Sons.

[S6] Wikipedia contributors (2023). Standard litre per minute — Wikipedia, the free encyclopedia. . https://en.wikipedia.org/wiki/Standard_litre_per_minute [Online; accessed 24-January-2024].

[S7] Tangirala, A.K. (2018). Principles of system identification: theory and practice. CRC press.

[S8] van Laake, L.C., de Vries, J., Malek Kani, S., and Overvelde, J.T.B. (2022). A fluidic relaxation oscillator for reprogrammable sequential actuation in soft robots. Matter *5*, 2898–2917. https://www.sciencedirect.com/science/article/pii/S2590238522002971. https://doi.org/10.1016/j.matt.2022.06.002.

[S9] van Laake, L.C., Comoretto, A., and Overvelde, J.T.B. (2024). On the coexistence of pressure regulation and oscillation modes in soft hysteretic valves. Journal of Fluids and Structures *126*, 104090. https://www.sciencedirect.com/science/article/pii/S0889974624000252. https://doi.org/10.1016/j.jfluidstructs.2024.104090.